

Flow-to-Friction Transition in Simulated Calcite Gouge: Experiments and Microphysical Modelling

André Niemeijer¹, J. Chen¹, and Berend Antonie Verberne²

¹Utrecht University

²Geological survey of Japan, AIST

November 21, 2022

Abstract

A (micro)physical understanding of the transition from frictional sliding to plastic or viscous flow has long been a challenge for earthquake cycle modelling. We have conducted ring-shear deformation experiments on layers of simulated calcite fault gouge under conditions close to the frictional-to-viscous transition previously established in this material. Constant velocity (v) and v -stepping tests were performed, at 550 @C, employing slip rates covering almost six orders of magnitude (0.001 - 300 $\mu\text{m/s}$). Steady-state sliding transitioned from (strong) -strengthening, flow-like behavior to -weakening, frictional behavior, at an apparent ‘critical’ velocity (v_c) of $\sim 0.1 \mu\text{m/s}$. Velocity-stepping tests using $v < v_c$ showed ‘semi-brittle’ flow behavior, characterized by high stress-sensitivity (n -value) and a transient response resembling classical frictional deformation. For $v > v_c$, gouge deformation is localized in a boundary shear band, while for $v < v_c$, the gouge is well-compacted, displaying a progressively homogeneous structure as the slip rate decreases. Using mechanical data and post-mortem microstructural observations as a basis, we deduced the controlling shear deformation mechanisms, and quantitatively reproduced the steady-state shear strength-velocity profile using an existing micromechanical model. The same model also reproduces the observed transient responses to v -steps within both the flow-like and frictional deformation regimes. We suggest that the flow-to-friction transition strongly relies on fault (micro-)structure and constitutes a net opening of transient micro-porosity with increasing shear strain rate at $v < v_c$, under normal-stress-dependent or ‘semi-brittle’ flow conditions. Our findings shed new insights into the microphysics of earthquake rupture nucleation and dynamic propagation in the brittle-to-ductile transition zone.

Flow-to-Friction Transition in Simulated Calcite Gouge: Experiments and Microphysical Modelling

Jianye Chen^{1,2,*}, B. A. Verberne³, and A. R. Niemeijer¹

¹ HPT Laboratory, Department of Earth Sciences, Utrecht University, the Netherlands

² Faculty of Civil Engineering and Geosciences, Technical University of Delft, Delft, the Netherlands

³ Geological Survey of Japan, National Institute of Advanced Industrial Science and Technology, Tsukuba, Japan

* Corresponding author: Jianye Chen (e-mail: j.chen3@uu.nl)

Address: Princetonlaan 4, 3584 CB Utrecht, The Netherlands

Key Points:

- We present a transition from flow to friction with increasing slip rate for a simulated carbonate fault sheared at 550 °C.
- A microphysically-based model reproduces the lab-observed flow-to-friction transition, including the transient frictional/flow behaviors
- Faults exhibit semi-brittle flow behavior by creep cavitation prior to earthquake rupture at the BDT zone, which serves as precursory phase.

Key words:

Calcite friction, Flow-to-friction transition, brittle-to-ductile transition, microphysical model, earthquake nucleation, rock deformation mechanisms

Abstract

A (micro)physical understanding of the transition from frictional sliding to plastic or viscous flow has long been a challenge for earthquake cycle modelling. We have conducted ring-shear deformation experiments on layers of simulated calcite fault gouge under conditions close to the frictional-to-viscous transition previously established in this material. Constant velocity (v) and v -stepping tests were performed, at 550 °C, employing slip rates covering almost six orders of magnitude (0.001 – 300 $\mu\text{m/s}$). Steady-state sliding transitioned from (strong) v -strengthening, flow-like behavior to v -weakening, frictional behavior, at an apparent ‘critical’ velocity (v_{cr}) of $\sim 0.1 \mu\text{m/s}$. Velocity-stepping tests using $v < v_{cr}$ showed ‘semi-brittle’ flow behavior, characterized by high stress-sensitivity (n -value) and a transient response resembling classical frictional deformation. For $v \geq v_{cr}$, gouge deformation is localized in a boundary shear band, while for $v < v_{cr}$, the gouge is well-compacted, displaying a progressively homogeneous structure as the slip rate decreases. Using mechanical data and post-mortem microstructural observations as a basis, we deduced the controlling shear deformation mechanisms, and quantitatively reproduced the steady-state shear strength-velocity profile using an existing micromechanical model. The same model also reproduces the observed transient responses to v -steps within both the flow-like and frictional deformation regimes. We suggest that the flow-to-friction transition strongly relies on fault (micro-)structure and constitutes a net opening of transient micro-porosity with increasing

43 shear strain rate at $v < v_{cr}$, under normal-stress-dependent or ‘semi-brittle’ flow conditions. Our
44 findings shed new insights into the microphysics of earthquake rupture nucleation and dynamic
45 propagation in the brittle-to-ductile transition zone.

46

47 1. Introduction

48 Within the seismogenic zone and above, fault displacement is achieved by frictional shear
49 deformation, whereas at much deeper levels in the crust this dominantly occurs by
50 thermally-activated creep mechanisms. Under “fully-plastic”, “-ductile”, or “-viscous” conditions,
51 creep flow is fast enough to inhibit unstable fault rupture (Scholz, 1988; Meissner & Strehlau,
52 1982). The transition with increasing depth (or temperature) from frictional fault slip to
53 fully-plastic flow is gradual, involving a competition between time-insensitive (e.g. granular flow)
54 and thermally activated time-sensitive (creep) deformation mechanisms over a depth range of
55 several km’s, or a few tens to hundreds of degrees Celsius (e.g., Kawamoto & Shimamoto, 1997;
56 Holdsworth et al. 2001; Imber et al. 2008; Bos & Spiers, 2002; Niemeijer & Spiers, 2006). This
57 depth interval, termed the “frictional-viscous” or “brittle-to-ductile transition” (BDT) zone, is
58 characterized by aseismic as well as seismic fault motion, as implied by field observations of
59 coexisting mylonites and pseudotachylytes (e.g., Stipp et al., 2002; Ueda et al., 2008; Bestmann et
60 al., 2012; Hayman & Lavier, 2014). A comprehensive understanding of the (micro)physical
61 processes leading to fault rupture, is needed to improve numerical models of earthquake fault
62 dynamics within and beyond the BDT (Tse & Rice 1986; Shimamoto & Noda, 2014; Jiang &
63 Lapusta, 2016).

64 To capture the frictional-viscous or BDT quantitatively and construct or test a constitutive
65 law, a dataset covering a wide range of slip velocities and temperatures is key. Synthetic and
66 natural fault rocks with composite mineralogical compositions (e.g., halite- and
67 quartz-phyllosilicate mixtures) as well as natural fault gouges exhibit transitional shear
68 deformation behavior from frictional slip to viscous flow with decreasing slip rate (e.g.,
69 Shimamoto, 1986; Chester & Higgs, 1992; Blanpied et al., 1995; Bos & Spiers, 2002; Noda &
70 Shimamoto, 2010; den Hartog & Spiers, 2013; Niemeijer et al., 2016, 2018). To our knowledge,
71 powdered halite remains thus far the only simulated fault rock for which the complete transition
72 from friction to flow with decreasing slip rate has been demonstrated experimentally (Shimamoto,
73 1986; Chester, 1988). This is important, because laboratory simulations combined with
74 (post-mortem) microstructural observations enable systematic investigation of the microphysical
75 processes controlling the BDT.

76 Verberne et al. (2015, 2017) conducted ring shear experiments on layers of simulated
77 calcite fault gouge at temperatures (T) of 20 - 600 °C and effective normal stresses (σ_n) up to 120
78 MPa. At a normal stress, σ_n , of 50 MPa, transitions with increasing temperature were observed
79 from stable (aseismic), v -strengthening to potentially unstable (seismogenic), v -weakening at ~100
80 °C, and back to stable, v -strengthening at ~600 °C. The latter transition, from unstable to stable
81 slip at high temperatures, was interpreted to represent a change from frictional deformation in
82 localized, porous slip zones to (more) distributed, dense ductile flow. Existing constitutive models
83 follow an ad-hoc approach, connecting the strength envelopes of empirical friction and flow laws
84 (Brace & Kohlstedt, 1980; Reinen et al., 1992; Chester & Higgs, 1992; Beeler, 2009; Shimamoto
85 & Noda, 2014), or else by introducing an empirical T -dependence (Chester, 1994) or an evolution
86 of grain contact area (Aharonov & Scholz, 2018, 2019) to the rate-and-state dependent friction

87 (RSF) laws. However, a fully microphysically-based constitutive model, calibrated to
88 (post-mortem) microstructural observations, is lacking.

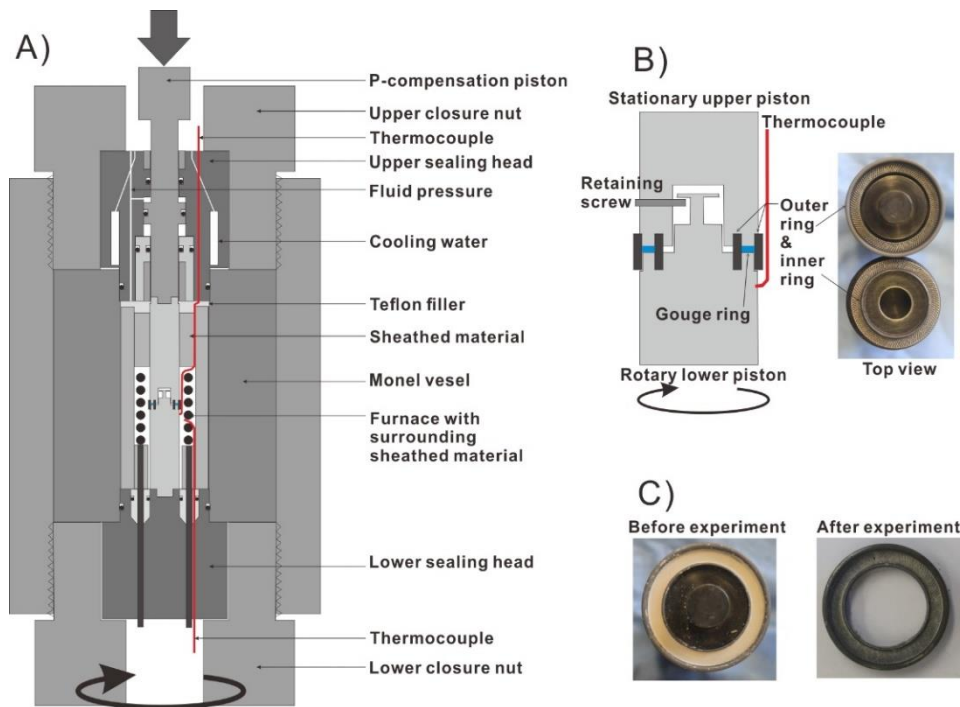
89 We investigate the mechanical and microstructural characteristics of the
90 frictional-to-viscous (or brittle-to-ductile) transition in simulated calcite gouge, at $T = 550$ °C and
91 $\sigma_n = 50$ MPa, using displacement rates spanning 6 orders of magnitude. Our aim was to document,
92 for the first time, the complete flow-to friction-transition with increasing slip velocity in simulated
93 fault rock composed of monomineralic calcite. We employed a microphysically-based constitutive
94 model for shear of gouge-filled faults (the CNS model; Niemeijer & Spiers, 2007; Chen & Spiers,
95 2016; Chen et al., 2017; Chen & Niemeijer, 2017; Chen et al., 2020) to quantitatively explain the
96 experimentally observed, steady-state and transient friction/ flow behavior. Specifically, we link
97 fault shear strength to internal changes in porosity with increasing displacement, controlled by the
98 competition between intergranular dilatation by granular flow and creep-controlled compaction.
99 Using our experimental and microstructural observations as a basis, combined with microphysical
100 modelling, we discuss implications for fault slip behavior within the BDT zone.

101

102 **2. Materials and Methods**

103 **2.1. Material and Deformation Apparatus**

104 We conducted experiments on simulated fault gouges composed of pure calcite, using the
105 hydrothermal ring shear apparatus installed at Utrecht University (Fig. 1A). Simulated calcite
106 gouge was prepared from crushed, Iceland Spar (CaCO_3) single crystals, sieved to a particle size
107 fraction of less than 28 μm (the same as used by Verberne et al., 2015, 2017). X-ray diffraction
108 analysis showed the calcite gouge to consist of 98% calcite, with minor ($\leq 2\%$) dolomite. In each
109 experiment, ~ 0.65 g of calcite powder was distributed in the annular space between two grooved
110 René-41 Ni-alloy pistons and confined by an outer and an inner ring with a diameter of 28 mm
111 and 22 mm, respectively (Fig. 1B, C). To reduce wall friction, the confining rings were lubricated
112 using Molykote D-321R anti-friction coating. In our experiments we measured shear displacement
113 using a potentiometer attached to the pressure vessel. Displacement normal to the shearing
114 direction (i.e., compaction/dilatation) was measured using a linear variable differential transducer
115 attached to the Instron frame. For more details on the apparatus we refer to Niemeijer et al. (2008,
116 2016).



117

118 Figure 1. The Utrecht ring-shear hydrothermal pressure vessel and sample assembly used. a) Cross
 119 section of the pressure vessel, b) blow up of the sample-piston assembly including the top view of the
 120 pair of pistons and confining rings, and c) simulated gouge layers before and after a shear experiment.

121

122 2.2. Experimental Conditions, Procedures, and Data analysis

123 All experiments were conducted at a temperature (T) of 550 °C, an effective normal stress (σ_n)
 124 of 50 MPa, and a pore fluid pressure (P_f) of 100 MPa (the same T - σ_n - P_f) conditions as used by
 125 Verberne et al. (2017). We used a constant sliding velocity (v) ranging between 0.027 $\mu\text{m/s}$ and
 126 300 $\mu\text{m/s}$, or else we employed sequentially stepped values in the range from 0.001 to 300 $\mu\text{m/s}$.
 127 Our experiments achieved total shear displacements (x) ranging between 5.4 mm and 10.2 mm.
 128 The test conducted at $v = 0.027 \mu\text{m/s}$ ran for ~56 hours. Even lower shear displacement rates were
 129 achieved by adding an additional gear box to the rotational drive system. This was used in ~3-fold,
 130 downward-only v -stepping tests with an initial v of 0.1 $\mu\text{m/s}$ (i.e., $v = 0.1 \rightarrow 0.03 \rightarrow 0.01 \rightarrow 0.003$
 131 $\rightarrow 0.001 \mu\text{m/s}$), except one test using 0.1 $\rightarrow 0.03 \mu\text{m/s}$. We imposed downward-only v -steps with
 132 the aim to avoid shear strain localization effects in the sample at low strains in the experiment. We
 133 also conducted v -stepping tests covering relatively high slip rates, using 3-fold and 1.75-fold steps
 134 in the range from 0.1 $\mu\text{m/s}$ to 300 $\mu\text{m/s}$. Table 1 shows a list of the v -step sequences imposed in
 135 each experiment.

136 Upon terminating an experiment, we first removed the shear stress by rotating the vessel
 137 including lower internal piston in the opposite direction, at 1 $\mu\text{m/s}$, followed by a decrease of the
 138 normal stress to ~4.2 MPa (= 1 kN normal load). To prevent vaporization of pore water, we
 139 gradually lowered the temperature while simultaneously maintaining the fluid pressure above ~22
 140 MPa (i.e., the supercritical pressure of water, and see a represent annealing curve in the
 141 Supplement). Upon reaching $T < 100 \text{ }^\circ\text{C}$, the vessel was depressurized to atmospheric conditions,
 142 the remaining normal load was removed, and the piston-sample assembly was disassembled. In
 143 total, it took about 45 minutes between termination of the experiment and removal of the sample
 144 from the pressure vessel.

145 In the ring-shear apparatus the confining rings are unsealed, so the fluid present in the
146 pressure chamber (demineralized water) has direct access to the sample, and acts as a pore fluid.
147 The piston-sample assembly is fluid pressure-compensated (Fig. 1A), so that the effective normal
148 stress (σ_n) acting on the sample layer can be calculated directly from the applied normal load,
149 minus a contribution from the O-ring seals (~ 2.85 MPa). The externally measured torque was
150 corrected for dynamic seal friction using displacement- and pore pressure-dependent calibrations
151 following Den Hartog et al. (2013). The shear stress (τ) supported by the sample was determined
152 assuming a uniform load distribution over the width of the annular sample (3 mm). Standard error
153 propagation analysis showed that $\delta\tau \leq 0.1\%$. Experiments which employed relatively low
154 displacement rates ($v < 1 \mu\text{m/s}$) spanning relatively long durations (> 20 hours), showed
155 fluctuations in τ resulting from poor temperature control (± 3 °C worst case). The steady-state shear
156 stress (or shear strength, τ_{ss}) was determined as the average τ -value over a 2 – 4 mm slip interval,
157 with the uncertainty being twice the standard deviation. The friction coefficient (μ) was calculated
158 by dividing the shear stress by the seal friction-corrected σ_n -value, ignoring cohesion of the
159 sample layer (i.e., $\mu = \tau/\sigma_n$).

161 2.3. Sample Recovery and Microstructural Analysis Methods

162 For each experiment, recovered sample fragments were impregnated using an epoxy resin,
163 left to harden for several days, and used to prepare polished thin sections in an orientation normal
164 to the shear plane and (sub-)parallel to the shear direction. Each sectioned sample was first
165 analyzed using a Leica polarizing-light microscope, in transmitted light. Selected sections were
166 subsequently investigated using a FEI Helios Nanolab G3, or a Zeiss Sigma-0380 scanning
167 electron microscope (SEM). To enable conduction in the SEM, the sectioned samples were
168 sputter-coated with a ~ 7 nm thick layer of Pt/Pd. Because our samples are composed almost
169 entirely of calcite, we found that imaging in secondary electron (SE) mode was more effective
170 compared with backscattered electron (BSE) mode. Imaging was achieved with an acceleration
171 voltage of 5 to 10 kV and a beam current of 0.2 to 1.6 nA. Selected SE micrographs were analyzed
172 using the linear intercept method to obtain the grain size (d) distribution, assuming $d = 1.5L$ where
173 L is the measured apparent grain diameter as observed in our sectioned samples (following Gifkins,
174 1970).

175 To investigate the crystallographic orientation distribution of the calcite grains after shear
176 deformation we conducted electron backscatter diffraction (EBSD) analysis, using an Oxford
177 Instruments (OI) EBSD detector mounted on the Zeiss Sigma-0380 SEM. Prior to EBSD
178 measurements we re-polished the sections with a silica colloid, followed by coating with a carbon
179 film of less than 4.0 nm thickness. Automated EBSD mapping of rectangular areas $\sim 25 \mu\text{m} \times 25$
180 μm to $1 \text{ mm} \times 0.5 \text{ mm}$ in size was carried out employing an accelerating voltage of 15 to 20 kV,
181 beam current of ~ 2 nA, an aperture of $50 \mu\text{m}$, a working distance of ~ 20 mm, and a step size
182 ranging from 0.35 to $2.0 \mu\text{m}$ depending on the (average) grain size of the mapped area. The
183 Kikuchi band pattern at each measurement or pixel was automatically indexed using OI AZtec
184 software. Indexing in maps of the bulk sample was relatively successful (indexing success rate
185 (ISR) of 50 – 88%). However, within shear bands, indexing was relatively poor (ISR < 20 %),
186 even for the lowest step-size employed. For each EBSD map we carried out repeat measurements
187 in 2 or 3 corresponding areas of the sample. Crystallographic orientation data are plotted in upper
188 hemisphere, equal area, stereographic projections, with contours of mean uniform density (MUD)

189 generated using a half width of 15° and cluster size of 5° .

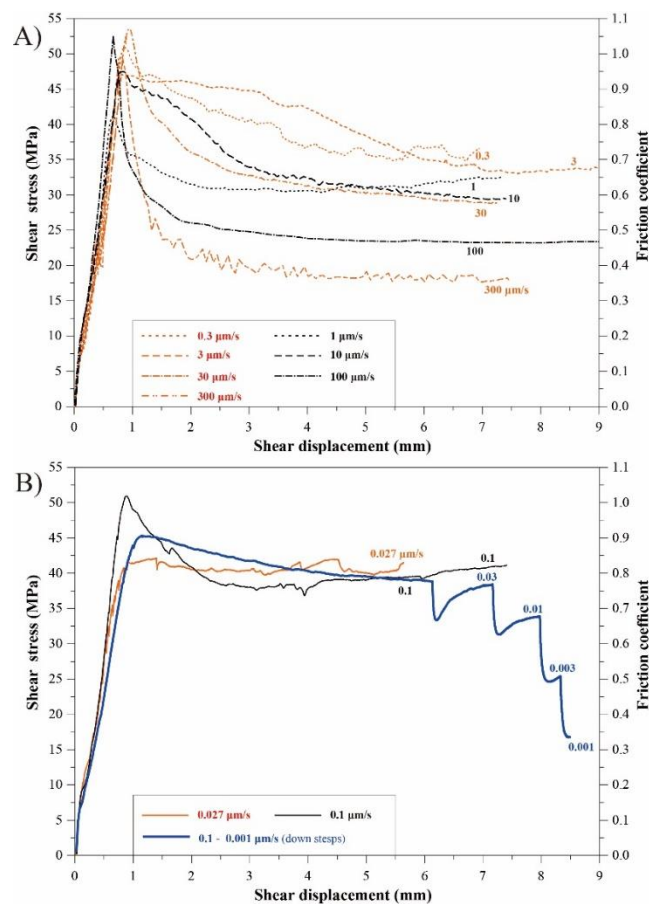
190

191 3. Results

192 3.1. Mechanical Data

193 We plot the shear stress τ (or friction coefficient μ) versus shear displacement x in Figure 2.
 194 All experiments and key parameters are listed in Table 1. For each experiment conducted using $v >$
 195 $0.1 \mu\text{m/s}$ the curves show rapid, near-linear loading in the first ~ 0.5 mm of shear displacement, a
 196 well-defined peak friction value of ~ 1.0 at $x \approx 0.5$ - 1.1 mm, followed by rapid, near-exponential
 197 decay to a steady-state friction value achieved after $x \approx 4$ - 5 mm (Fig. 2A). By contrast, for
 198 experiments using $v \leq 0.1 \mu\text{m/s}$, initial, near-linear loading was followed by apparent ‘yield’,
 199 gradual hardening to a maximum friction value, and either gradual weakening or else steady-state
 200 sliding at a near-constant shear strength value (Fig. 2B).

201



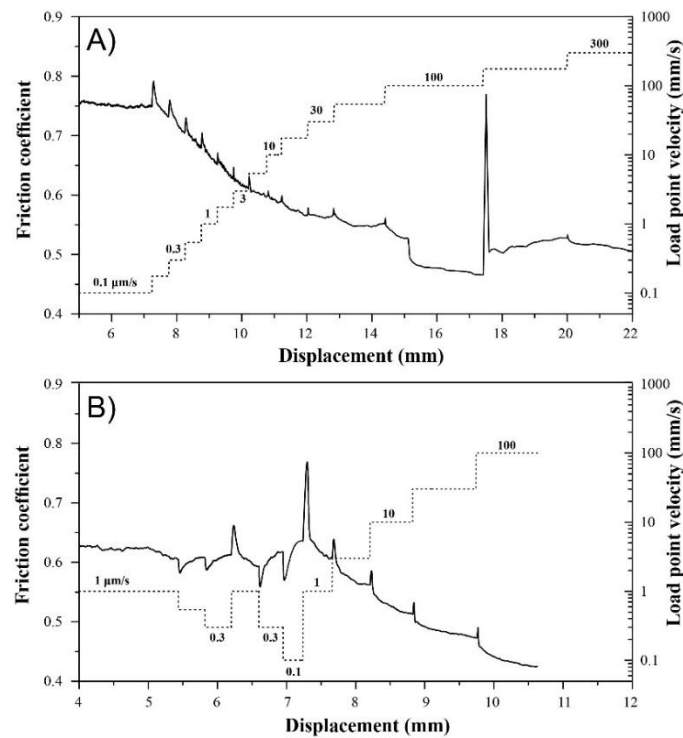
202

203 Figure 2. Rotary shear experiments on layers of simulated calcite fault gouge conducted at 550°C ,
 204 100 MPa fluid pressure, and 50 MPa effective normal stress conditions. The tests were run at
 205 constant velocities (v) falling in the range from 0.027 to $300 \mu\text{m/s}$. Result from a downward v -step
 206 experiment was added (in thick blue line), giving the steady states for v from $0.1 \mu\text{m/s}$ to 0.001
 207 $\mu\text{m/s}$. For better illustration, the results were only plotted to a shear displacement of 9.0 mm, and
 208 the data were separated into a) with $v > 0.1 \mu\text{m/s}$ and b) with $v \leq 0.1 \mu\text{m/s}$.

209

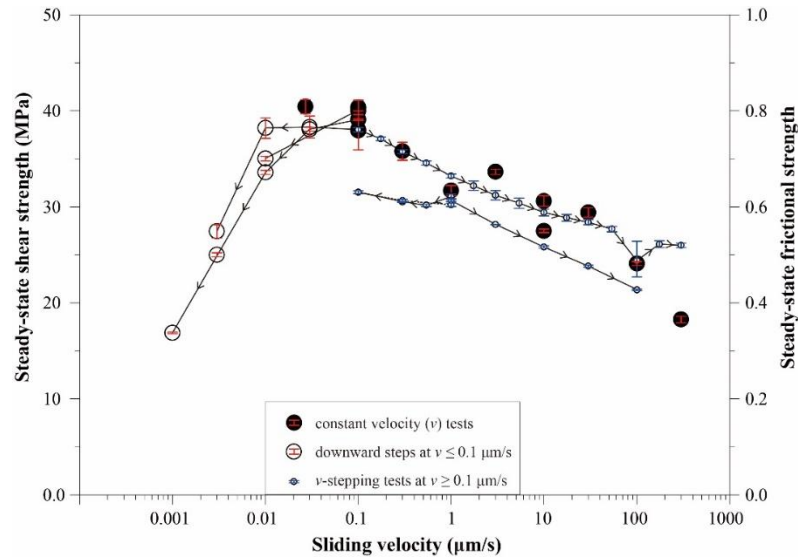
210 For the v -stepping experiment conducted using $v \leq 0.1 \mu\text{m/s}$ (u605), the strength values
 211 observed at the peak and at steady-state during initial sliding at $v = 0.1 \mu\text{m/s}$, are broadly

212 consistent with those observed in the constant- v experiment (u516, Fig. 2b). Downward steps in v
 213 consistently triggered a sharp drop in shear resistance, followed by gradual re-strengthening to a
 214 markedly lower, steady-state strength value (Fig. 2b), implying strong v -strengthening behavior.
 215 In the upward v -stepping tests conducted using $v \geq 1.0 \mu\text{m/s}$, each individual step showed
 216 ‘classical’ rate-and-state-friction (RSF) behavior, that is, a direct increase in μ -value followed by
 217 an exponential decay to a new steady state μ_{ss} (Fig. 3; for background on RSF theory see e.g.,
 218 Marone, 1998). For all the v -steps investigated, μ_{ss} consistently showed negative rate dependence
 219 (i.e., $d(\Delta\mu_{ss})/d(\ln v) < 0$), or v -weakening behavior. The ‘peak’ direct effect, in RSF known as the
 220 ‘ a ’-value, decreases with increasing v (Figs. 3A, B). At lower velocities, the slip distance required
 221 to re-attain steady-state sliding (‘ D_c ’ in RSF) is observed to increase, with the v -steps at low
 222 displacements not reaching steady state within $\sim 0.5 \text{ mm}$ slip interval. During the interval at $v =$
 223 $100 \mu\text{m/s}$ (experiment u502), sudden, drastic weakening occurred, followed by an extraordinarily
 224 large direct effect when stepping to $300 \mu\text{m/s}$ (Fig. 3A). Similar drastic weakening at $v = 100 \mu\text{m/s}$
 225 was also reported by Verberne et al. (2015).
 226



227
 228 Figure 3. Results from two velocity-stepping tests in the high velocity range ($0.1 - 100 \mu\text{m/s}$). The
 229 experimental conditions are the same as that in Figure 2.

230
 231 Mean values of the steady-state shear strength (τ_{ss}) or μ_{ss} ($= \tau_{ss}/\sigma_n$) from the constant- v and the
 232 v -stepping experiments are plotted against $\log(v)$ in Figure 4. In both types of experiments, the
 233 uncertainty in the shear strength measurements ($\Delta\tau_r$, indicated by the error bars in Fig. 4) is less
 234 than $\pm 1.3 \text{ MPa}$, except for the data obtained at $v = 100 \mu\text{m/s}$ in v -stepping test u502 for which $\Delta\tau_r$
 235 $= \pm 2.3 \text{ MPa}$. In general, data from all experiments are consistent, pointing to a transition with
 236 increasing v in the sign of $d\mu_{ss}/d\log(v)$, from positive to negative, around a ‘critical’ velocity (v_{cr})
 237 of $\sim 0.1 \mu\text{m/s}$.
 238



239

240 Figure 4. Steady-state shear strength as a function of sliding velocity for a simulated calcite fault
 241 gouge sheared at 550 °C and 50 MPa effective normal stress conditions. Data are derived from the
 242 experiments shown in Figures 2 and 3, and another two from Verberne et al., (2017) (see Table 1
 243 for details). The red bars give the errors to steady-state shear strength for individual velocity steps.

244

245 3.2. Microstructures

246 Upon sample recovery after an experiment we found that samples that were sheared at low v
 247 ($\leq 0.1 \mu\text{m/s}$) could be extracted as a single, coherent piece, whereas samples sheared at high v ($>$
 248 $0.1 \mu\text{m/s}$) typically broke along shear plane-parallel and inclined shear fractures, resulting in
 249 multiple arc-shaped fragments. Transmitted light micrographs of sections prepared from each
 250 experiment are shown in Supplementary Figure S1. Below we describe the microstructures of
 251 representative samples u605, u508, and u635, which were deformed using final displacement rates
 252 in the experiment (v_{final}) of respectively $0.001 \mu\text{m/s}$, $0.03 \mu\text{m/s}$, and $10 \mu\text{m/s}$ (see Table 1).

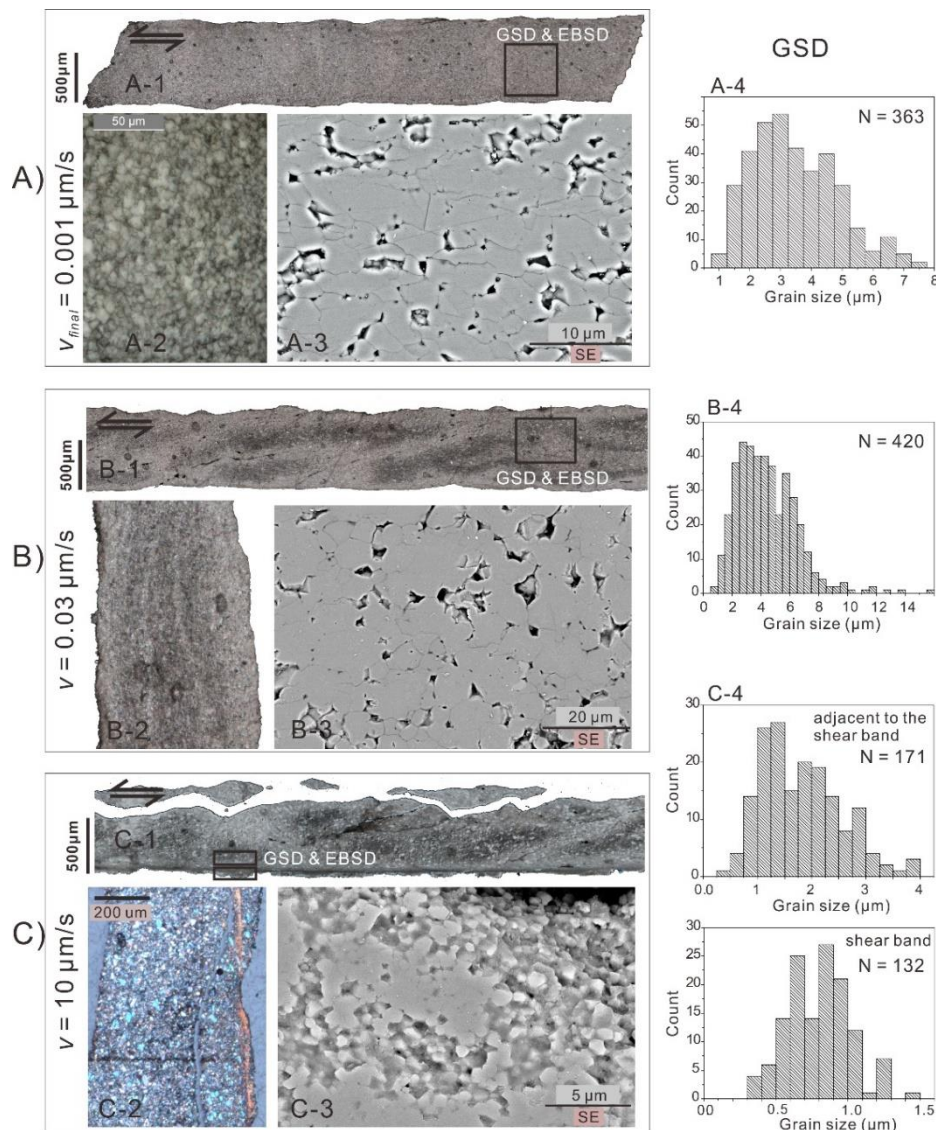
253

254 3.2.1. Light and Electron Microscope Observations

255 Sample u605 ($v_{final} = 0.001 \mu\text{m/s}$) showed a dense, near-uniform microstructure composed of
 256 apparently rounded grains as observed under plane polarized light (PPL) (Fig. 5A, see also Fig.
 257 S1). We observed no evidence for localization of shear deformation. Secondary electron (SE)
 258 micrographs revealed that the sample is characterized by densely-packed polygonal grains,
 259 frequently with $\sim 120^\circ$ triple junctions (Fig. 5A). Occasionally, the grains are elongated, with a
 260 long axis oriented (sub-) parallel to the shear plane (Fig. 5A). The grain size distribution (GSD)
 261 has a range of $d = 1.0 - \sim 7.0 \mu\text{m}$ ($N = 363$), and a mean (\bar{d}) of $\sim 3 \mu\text{m}$. Sample u508 ($v_{final} = v =$
 262 $0.03 \mu\text{m/s}$) showed light- and dark-grey bands oriented parallel and inclined to the shear plane and
 263 -direction, as observed using PPL (Fig. 5B). We infer that these bands are an artifact from section
 264 preparation, possibly representing different degrees of epoxy impregnation. SE micrographs show
 265 that this sample has an overall dense microstructure with widespread polygonal grains, resembling
 266 the microstructure of sample u605 which was sheared at $v_{final} = 0.001 \mu\text{m/s}$ (cf. Fig. 5A). The GSD
 267 ($N = 420$) has a range $d = 1$ to $14 \mu\text{m}$ and $\bar{d} = 4 \mu\text{m}$.

268 Microstructures of samples that were sheared using $v_{final} > 1.0 \mu\text{m/s}$ consistently showed the
 269 presence of a ~ 20 to $60 \mu\text{m}$ wide, shear-plane parallel zone composed of ultra-finely comminuted

270 grains, located along at least one of the sample boundaries. For most samples, this boundary (B)
 271 shear band was only partially recovered. Light microscope observations of sample u635 ($v_{final} = v$
 272 $= 10 \mu\text{m/s}$), under crossed-polarized light (XPL) using the gypsum plate inserted, revealed that the
 273 B-shear is characterized by a strong uniform birefringence and optical extinction, suggestive of a
 274 crystallographic preferred orientation (CPO) (Fig. 5C). Using a light microscope grains within the
 275 B-shear cannot be resolved, whereas in the adjacent bulk gouge, the grains are angular, randomly
 276 packed, and have a size-range close to that of the starting material ($d = 0.7 - 50 \mu\text{m}$, with $\bar{d} = 20$
 277 μm , Fig. 5C-1). SE micrographs revealed that the B-shear is relatively porous for most portions
 278 ($\sim 3\text{-}7\%$), and that the grains are polygonal to rounded with d in the range from 0.3 to 1.5 μm , and
 279 $\bar{d} = 0.8 \mu\text{m}$ (cf. Fig 5C-3 and 5A-3).



280

281 Figure 5. Microstructure of layers of simulated calcite fault gouges from three experiments, sheared at
 282 A) $v_{final} = 0.001 \mu\text{m/s}$ (u605), B) constant- $v = 0.03 \mu\text{m/s}$ (u608), and C) constant- $v = 10 \mu\text{m/s}$ (u635),
 283 respectively. Each sample is displayed in four panels: (panels A-1, B-1, and C-1), a transmitted light
 284 photomosaic of thin section over the entire gouge layer thickness; (panels A-2, B-2, and C-2), an
 285 exaggerated area of potential interests; (panels A-3, B-3 and C-3), a SEM image of a representative
 286 area or the shear band if present; and (panels A-4, B-4, C-4), a histogram of grain size distribution for

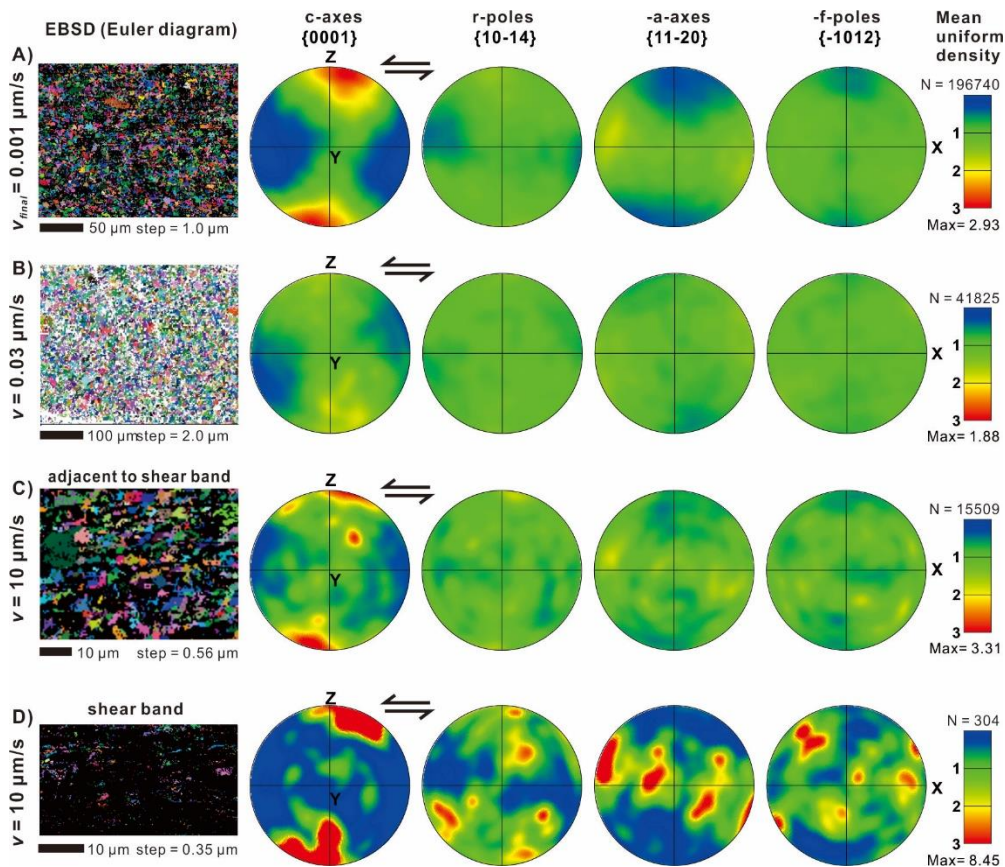
287 the selected area. Note that the image shown in Panel C2 was taken using cross polarized light with the
 288 gypsum plate inserted. For each sample, imaged-based grain size distribution analysis was performed
 289 on selected area as marked in rectangles in panels A-1, B-1 and C-1. For the sample sheared at 10 $\mu\text{m/s}$,
 290 these analyses were performed in both the shear band and the adjacent area.

291

292 3.2.2. Electron Backscatter Diffraction Analyses

293 EBSD mapping was carried out of samples u605, u508, and u635, which were deformed at
 294 respectively $v_{final} = 0.001 \mu\text{m/s}$, $0.03 \mu\text{m/s}$ and $10 \mu\text{m/s}$ (see Table 1). All maps recorded in ‘slow’
 295 experiments u605 and u508 ($v < 0.1 \mu\text{m/s}$) showed $\text{ISR} \geq 70\%$ (Figs. 6A, B and see results from
 296 more areas in Figs. S2A, B). By contrast, for maps prepared from sample u635, $\text{ISR} \leq 61\%$, with
 297 the lowest value of $\sim 20\%$ for a map of a B-shear band (Fig. 6D and Fig. S2D). Stereographic
 298 projections revealed strong c-axis maxima in sample u605 ($v_{final} = 0.001 \mu\text{m/s}$, Fig. 6A), and in the
 299 bulk part of sample u635 ($v_{final} = v = 10 \mu\text{m/s}$, Fig. 6C), but less so in sample u508 ($v_{final} = v = 0.03$
 300 $\mu\text{m/s}$). For the shear band in sample u635, as evident from the Euler map in Figure 6D, the data
 301 are mostly from a few, relatively large grains. Due to poor indexing ($\text{ISR} \leq 20\%$) it remains
 302 difficult to compare these and other data obtained from B-shear bands with other samples.

303



304

305 Figure 6. Electron backscatter diffraction (EBSD) of simulated calcite fault gouges retrieved from three
 306 experiments, sheared at A) $v_{final} = 0.001 \mu\text{m/s}$ (u605), B) constant- $v = 0.03 \mu\text{m/s}$ (u608), and C), D)
 307 constant- $v = 10 \mu\text{m/s}$ (u635), respectively (see the mapped areas in Fig. 5). For sample u635, the
 308 analyses were performed in both the shear band and the adjacent area. The left panels give the Euler
 309 angle diagram of the mapping area. A step size of 1.0 or 2.0 μm was used in the mapping except for the
 310 shear band of u635, where a step size of 0.3 – 0.6 μm was taken. The EBSD data were plotted in upper

311 hemisphere, equal area pole diagrams for X, Y and Z directions, respectively.

312

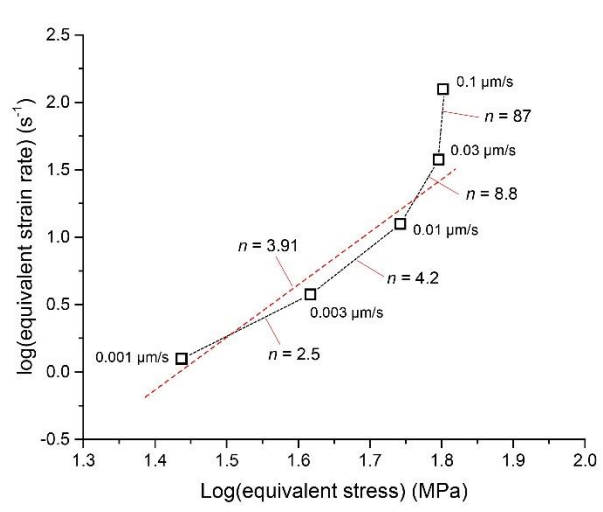
313 4. Data Analysis and Deformation Mechanisms

314 4.1. Mechanisms Controlling Shear Deformation at $v < 0.1 \mu\text{m/s}$

315 In view of the high temperature (550 °C) used in our experiments and the mechanical and
 316 microstructural observations reported above, it is reasonable to suppose that creep processes
 317 played at least some role in our experiments, especially at the low displacement rates ($v < 0.1$
 318 $\mu\text{m/s}$). To investigate this, and to identify a suitable constitutive equation that can be used to
 319 model our results, we compare the stress sensitivity of the ductile strain rate (the so-called
 320 “ n -value”) as derived from our low- v shear experiments with values determined from compression
 321 experiments on dense calcite polycrystals.

322 To this end, we first converted the steady-state shear stress (τ) and shear strain rate ($\dot{\gamma}$) in our
 323 experiments to an equivalent compressive flow (differential) stress (σ) and strain rate ($\dot{\epsilon}$), using $\dot{\epsilon}$
 324 $= \sqrt{3}\dot{\gamma}$ and $\sigma = \sqrt{3}\tau$ (Schmid et al., 1987). The ‘slowest’ experiments (u605, using $v_{final} = 0.001$
 325 $\mu\text{m/s}$) showed a near-homogeneously deformed microstructure (Figs. 5A). Taking a uniform shear
 326 zone width l of 0.8 mm, this implies that, in experiments using $v_{final} \leq 0.03 \mu\text{m/s}$, $\dot{\gamma} \approx 1.25 \times 10^{-6}$ to
 327 $3.75 \times 10^{-5} \text{ s}^{-1}$ and $\dot{\epsilon} \approx 2.17 \times 10^{-6}$ to $6.50 \times 10^{-5} \text{ s}^{-1}$. For each v -step interval in the experiment, we
 328 calculated $\dot{\gamma}$ and $\dot{\epsilon}$, assuming constant thickness $W = 0.8 \text{ mm}$ (Fig. 7). A generalized power law
 329 stress dependency of the compressive strain rate (i.e., $\dot{\epsilon} \propto \sigma^n$) implies $n = d\log(\dot{\epsilon})/d\log(\sigma)$,
 330 hence an estimate of the n -value can be obtained by taking the slope of the interpolated curve
 331 shown in Fig. 7. For each step, the corresponding n -value progressively decreases. Ignoring the
 332 first step, all values fall in the range from $n \approx 2.5$ to 8.8, with mean $\bar{n} \approx 3.91$, which falls between
 333 n -values reported for flow of dense calcite polycrystals by diffusion creep ($1.1 < n < 1.7$) and by
 334 dislocation creep ($4.2 < n < 7.6$) (see Table 2, see De Bresser et al. 2002 and references therein).
 335 The best match is with the n -value of 3.33 reported by Walker et al. (1990), who best-fit a
 336 composite, grain size- and stress-dependent flow law to data from compression experiments on
 337 synthetic, hot-pressed calcite aggregates conducted at $\sigma < 25 \text{ MPa}$ and $T = 400 - 700 \text{ °C}$. These
 338 authors suggested that grain size-sensitive (diffusion) and -insensitive (dislocation) creep occurred
 339 simultaneously in their experiments.

340



341

342 Figure 7. Equivalent strain rate ($\dot{\epsilon}$) versus equivalent stress (σ) in the logarithmic scale from the

343 experiment (u605), which was sheared with downward v -step sequence from 0.1 μm to 0.001 μm .
 344 Assuming a general creep law of a power law form ($\dot{\epsilon} \propto \sigma^n$), the n -value can be obtained using the
 345 relation $n = d\log(\dot{\epsilon})/d\log(\sigma)$ for all the steps, as indicated by the slopes.

346
 347 Based on the above, we posit that shear deformation at $v < 0.1 \mu\text{m/s}$ in our experiments
 348 occurred by a combination of diffusion and dislocation creep processes. Importantly, the operation
 349 of dislocation and diffusion creep is consistent with microstructural observations. Firstly, samples
 350 sheared at $v < 0.1 \mu\text{m/s}$ showed distributed shear deformation, a relatively low porosity ($< \sim 2\%$),
 351 and polygonal grains characterized by straight grain boundaries and high-angle triple junctions
 352 (Figs. 5A-3, 5B-3). The latter are consistent with microstructures formed in compression
 353 experiments on dense calcite polycrystals, which deformed by grain size sensitive creep (Schmid
 354 et al., 1977; Walker et al., 1990). Furthermore, the presence of 4-9 μm -sized elongated grains in
 355 sample u605 ($v_{final} = 0.001 \mu\text{m/s}$; Fig. 5A) and the c-axis maximum (Fig. 6A, C) are suggestive of
 356 intracrystalline plasticity (cf., Walker et al., 1990; Lafrance et al., 1994; Schmid et al., 1987;
 357 Rutter et al., 1994). Lastly, the grain size distribution measured in samples sheared at $v_{final} < 0.1$
 358 $\mu\text{m/s}$ is much narrower than compared with that in the starting material (ranging 1–9 vs 0.7–50
 359 μm), implying that dynamic and or static recrystallization played a role in our experiment (Drury
 360 et al. 1985). A simple calculation using the equation given by Covey-Crump (1997) for
 361 fluid-assisted grain growth in dense calcite aggregates with $d < 10 \mu\text{m}$, indicates that, in our ‘slow’
 362 experiments using $v \leq 0.1 \mu\text{m/s}$, grain growth is only expected in the first few hours ($< 10^4 \text{ s}$) of
 363 the experiments. Therefore, this process did not affect our steady-state data.

364 Combining all of the above, our interpretation is that shear strain accommodation at $v < 0.1$
 365 $\mu\text{m/s}$ in our experiments occurred by a combination of diffusion and dislocation creep (hereafter
 366 referred to the flow regime). However, around the critical velocity v_{cr} , shear strain accommodation
 367 is characterized by a ‘brittle’ component, as indicated by the large stress exponent ($n \sim 87$) for $v =$
 368 0.03 - 0.1 $\mu\text{m/s}$ (Fig. 4; Brantut et al., 2013; Chen et al., 2020), and by the ‘friction-like’ transient
 369 response to a step in v (Fig. 2B; Noda & Shimamoto, 2010; Chester, 1988).

370 371 **4.2. Mechanisms Controlling Shear Deformation at $v > 0.1 \mu\text{m/s}$**

372 All experiments which explored $v > 1.0 \mu\text{m/s}$ showed v -weakening behavior (Fig. 4). As
 373 mentioned above, in these ‘fast’ experiments the transient response strongly resembled “classical”
 374 RSF behavior, and recovered sample fragments consistently showed evidence for shear strain
 375 localization in a narrow (20 - 60 μm), boundary-parallel (B) shear band (Fig. 5C, S1). The
 376 presence of a B-shear suggests that this accommodated the bulk of the imposed shear deformation
 377 (Takahashi et al., 2017; Verberne et al., 2017). Assuming a constant, average shear band thickness
 378 of $\sim 40 \mu\text{m}$, the internal shear strain rate measured $\sim 2.5 \times 10^{-2} \text{ s}^{-1}$ to 6 s^{-1} for $v = 1 - 300 \mu\text{m/s}$, which
 379 is ~ 6 orders of magnitude higher than that in experiments conducted using $v \leq 0.1 \mu\text{m/s}$.

380 The shear band consists of polygonal or rounded grains, resembling the grain cavitated arrays
 381 reported to have formed by Verberne et al 2017 in experiments conducted under similar T - σ_n - P_f
 382 conditions (Fig. 5C). This, combined with the relatively high shear strain rates acting within the
 383 shear bands, implies that granular flow must have played a role. However, plastic creep
 384 mechanisms likely also played some role. In view of the high temperatures in our fluid-saturated
 385 experiments (550 $^\circ\text{C}$), and small mean grain size in the B-shear bands compared with samples
 386 sheared at $v < 0.1 \mu\text{m/s}$, water-assisted diffusion creep ($\dot{\epsilon} \propto d^{-3}$) is an obvious candidate. On the

387 other hand, the presence of a CPO, as evident from uniform optical birefringence under a light
 388 microscope (Fig. 5C-2), is suggestive of dislocation creep. A c-axis maximum, similar to the one
 389 observed in the low- v experiments, was identified in grains adjacent to a B-shear (Fig. 6C and S2),
 390 consistent with that reported by Verberne et al. (2017) for internal shear band grains.

391 Combining all of the above, our interpretation is that in the flow regime ($v < 0.1 \mu\text{m/s}$) a
 392 combination of diffusion and dislocation creep played the dominant role, while at high slip rates
 393 ($v > 0.1 \mu\text{m/s}$, hereafter referred to as the friction regime) granular flow played an important role
 394 alongside plastic creep process.

395

396 5. Microphysical Modelling

397 In this section, we use a previously developed microphysical model for shear of granular
 398 media, the Chen-Niemeijer-Spiers (CNS) model, to simulate the mechanical behavior of calcite
 399 gouge observed in our experiments. The CNS model is capable of quantitatively reproducing
 400 steady-state and transient shear behavior, using physics-based input parameters derived from
 401 laboratory observations. Constitutive equations of the CNS model are given in the Supporting
 402 Information; for details on model development and implementation we refer to Niemeijer &
 403 Spiers (2007), Chen & Spiers (2016), Chen & Niemeijer (2017), and Chen et al. (2017).

404

405 5.1. Model Framework and Parameters Used

406 In section 4 we showed that, within the range of sliding velocities corresponding with the
 407 frictional regime ($v > 0.1 \mu\text{m/s}$) in our experiments, shear plane-parallel deformation of a gouge
 408 layer of thickness W occurs by the simultaneous operation of granular flow ($\dot{\gamma}_{gr}$) and intergranular
 409 plastic creep ($\dot{\gamma}_{pl}$). In the assumed model geometry, granular flow operates in a shear band of
 410 width W_{sb} , while intergranular creep may occur involving the entire gouge, including the shear
 411 band as well as the adjacent bulk layer (W_{bulk}) (see the Supplementary Information). The
 412 implication is that

$$413 \quad v = W_{sb}\dot{\gamma}_{gr} + W_{sb}\dot{\gamma}_{pl}^{sb} + W_{bulk}\dot{\gamma}_{pl}^{bulk} \quad (1)$$

414 where $W_{sb} + W_{bulk} = W$ and $\dot{\gamma}_{pl}^{sb}$ and $\dot{\gamma}_{pl}^{bulk}$ are the creep strain rates within respectively the
 415 shear band and the bulk layer, in the shear direction. For $v < 0.1 \mu\text{m/s}$, shear deformation is more
 416 homogeneous, hence $W \approx W_{sb}$ and $v = W\dot{\gamma}_{gr} + W\dot{\gamma}_{pl}$.

417 All parameters and values used in our simulations are listed in Table 3. The temperature and
 418 effective normal stress used followed the experimental conditions employed (i.e., $T = 550 \text{ }^\circ\text{C}$, $\sigma_n =$
 419 50 MPa). Layer thicknesses (W), grain size (d), and porosities (ϕ) were set in accordance with
 420 post-mortem microstructural observations, where relevant of the shear band and the bulk sample
 421 layer. To simulate flow behavior at low velocities ($v < 0.1 \mu\text{m/s}$), we assumed a homogeneous
 422 shear zone of $W = 800 \mu\text{m}$, with $d \approx 2 - 3 \mu\text{m}$. Conversely, at high velocities ($v > 0.1 \mu\text{m/s}$), we
 423 assumed $W_{sb} \approx 20 - 100 \mu\text{m}$, $W_{bulk} = 800 - W_{sb} [\mu\text{m}]$, and a grain size of respectively $0.8 \mu\text{m}$ and
 424 $5.0 \mu\text{m}$. To match the overall shear strength level observed in our experiments (Fig. 4), we
 425 assumed a reference grain boundary friction value $\tilde{\mu}^*$ of 0.43 at $v = 0.1 \mu\text{m/s}$, and a rate
 426 dependent coefficient ($a_{\tilde{\mu}}$) of 0.01 (Chen & Spiers, 2016). Porosity and shear stress need to be
 427 solved. For both zones we assumed a critical porosity ϕ_c of 40% (see Vermeer & De Borst, 1984)
 428 and a non-zero limit porosity ϕ_0 of 2% (see the Supplement Text S1 for details).

429 We used a flow stress- (σ -) and grain size- (d -) sensitive constitutive law to quantify the creep
 430 strain rate ($\dot{\epsilon}$), as calibrated to data from compression tests on dense calcite polycrystals by Walker

431 et al. (1990) (see Table 2):

$$432 \quad \dot{\epsilon} = A \exp\left(-\frac{E_a}{RT}\right) \frac{\sigma^n}{d^m}. \quad (2)$$

433 Here A is a pre-exponential constant ($\log A = 6.68 \text{ s}^{-1} \mu\text{m}^{-m} \text{MPa}^{-n}$), E_a is the activation energy
 434 (190 kJmol^{-1}), T is the temperature, R is the gas constant ($8.31 \text{ Jmol}^{-1} \text{K}^{-1}$), and $m = 1.33$ and n
 435 $= 3.33$ are empirical constants. In the CNS model we used this creep law for both normal and
 436 shear deformation, with slightly different pre-exponential constants ($A_n = A$ and $A_t = \sqrt{3}^{n+1} A$,
 437 where A_n and A_t are the constants for normal and shear components, respectively; see Text S1 for
 438 detailed description). A porosity function is used to account for changing porosity in the frictional
 439 regime (Niemeijer & Spiers, 2007).

440 To simulate transient behavior, the sheared gouge layer is modeled analogous to a
 441 spring-slider system, composed of a linear spring of stiffness K that is activated at a load point at
 442 velocity v_{imp} , assuming no inertia;

$$443 \quad \dot{\tau} = K(v_{imp} - v) \quad (3)$$

444 The constitutive equations of the CNS model (eq. S1-S5), together with the creep law (eq. 2) and
 445 kinematic equations for fault deformation (eq. 1 and 3), can be rewritten into a pair of ordinary
 446 differential equations (ODEs) that specify the rate of change of shear stress ($\dot{\tau}$) and porosity ($\dot{\phi}$).
 447 All ODEs are solved using the finite element package COMSOL.

448

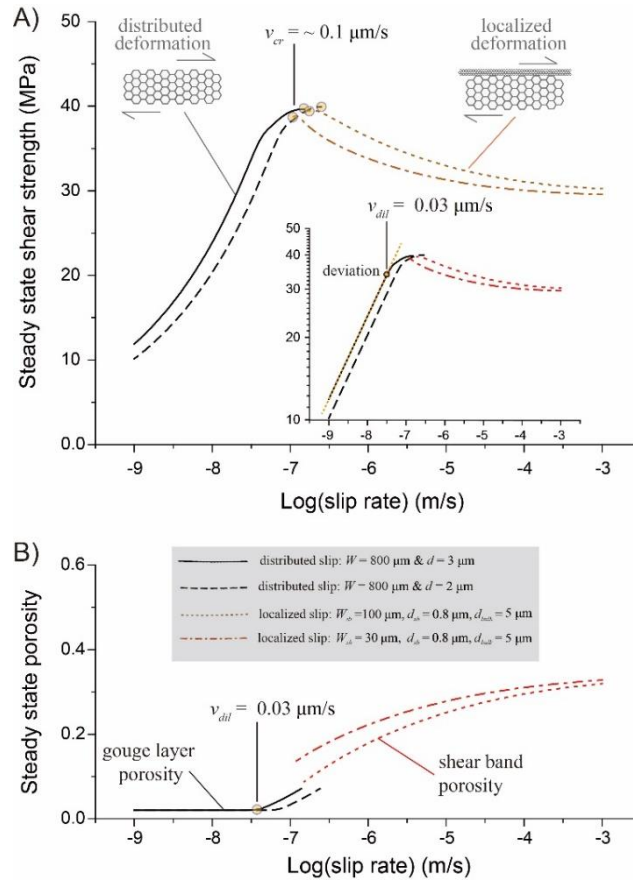
449 **5.2. Simulation Results and Comparison with Experiments**

450 **5.2.1. Steady-state Behavior**

451 The CNS model output simulating the steady-state shear strength and porosity change with
 452 increasing displacement in our experiments is shown in Fig. 8 and S4. We also carried out
 453 sensitivity analysis for grain size and shear band thickness. For a homogeneously shearing gouge
 454 layer at $v \leq 0.03 \mu\text{m/s}$, the model predicts strong v -strengthening behavior (Fig. 8A), reaching a
 455 ‘background’ (or limit) porosity ϕ_0 (Fig. 8B). When plotted in log-log space (Fig. 8A-inset), the
 456 τ - v curves are straight lines with $d\log(v)/d\log(\tau) = n = 3.3$ (see eq. 2). As v increases the
 457 steady-state porosity begins to increase from the background value, at the dilatation velocity $v_{dil} =$
 458 $\sim 0.03 \mu\text{m/s}$ (Fig. 8). This onset of dilatation, or, $\phi(v) > \phi_0$, is associated with a deviation of the τ - v
 459 curve from linearity (Fig. 8A-inset), implying a higher stress sensitivity (or larger ‘apparent’
 460 n -value). For $v > v_{cr} = 0.1 \mu\text{m/s}$, constituting localized shear, the model predicts persistent
 461 v -weakening and an increasing steady-state porosity with increasing v , with slopes that decrease
 462 with increasing v (Fig. 8). For each shear deformation regime ($v < v_{cr}$ and $v > v_{cr}$), the model
 463 outcome is generally consistent with the τ - v profile observed in the experiments (Fig. 8 cf. Fig. 4;
 464 see a detailed comparison in Fig. S4).

465 Regardless of the grain size or shear band width used, the τ - v curves show a smooth
 466 connection between both shear deformation regimes, that is, within a peak shear stress and
 467 velocity window of 38 to 40 MPa and 0.1 to 0.25 $\mu\text{m/s}$ (Fig. 8). However, there is a relatively
 468 large offset in porosity, which is unsurprising since the model assumes a different internal fault
 469 structure or geometry for the flow ($v < v_{cr}$) vs. the frictional ($v > v_{cr}$) regimes. The microphysical
 470 processes controlling the change from distributed to localized slip, at $v \sim v_{cr}$, is not captured by the
 471 present model. We note, however, that in the case that there would be no microstructural change at
 472 $v = v_{cr}$, the model predicts a continuous transition with increasing slip rate from v -strengthening to

473 v -weakening behavior (Fig. S5). This suggests that a flow-to-friction transition with increasing
 474 slip rate will always emerge from the model and that the microstructure controls the velocity at
 475 which the transition from v -strengthening to -weakening occurs (i.e., the value of v_{cr}).
 476
 477



478

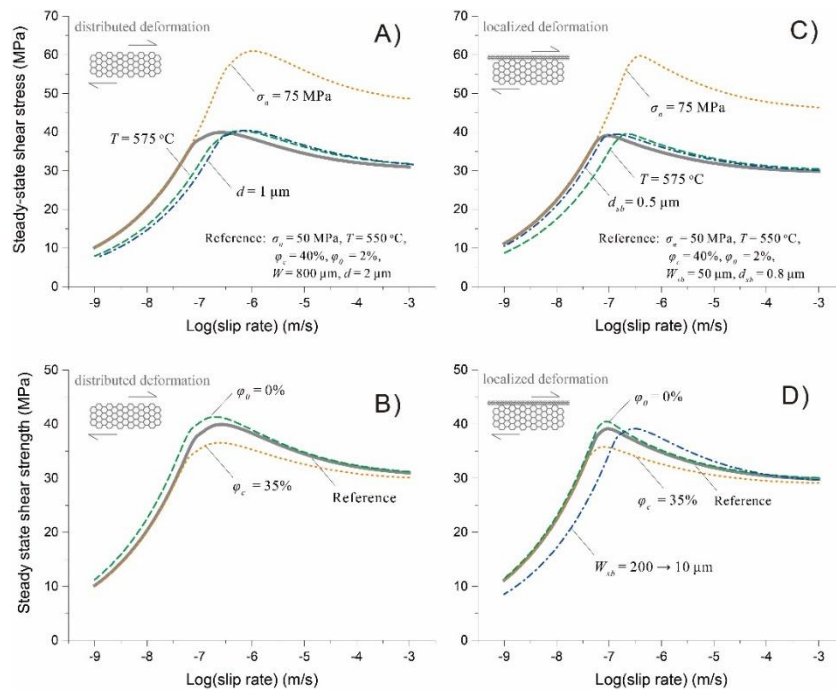
479 Figure 8. Steady-state A) shear strength and B) porosity as a function of slip velocity for a simulated
 480 calcite gouge layer at 550 °C and 50 MPa effective normal stress, predicted by the CNS model. The
 481 model conditions were set according to the experiments, with different model geometries resembling
 482 the microstructures observed at different slip rates. Specifically, for slow slip rates a uniform gouge
 483 layer was assumed, while at high slip rates, we assumed localized slip, with different grain sizes and
 484 thicknesses for the shear band and the bulk layer. The predicted results indicate in transition from flow
 485 to friction at a critical velocity (v_{cr}) of 0.1 μm , consistent with the observation. The inset graph of A)
 486 shows the same results but in the log-log scale, where the deviation from a linear line occurs at a
 487 velocity corresponding to the onset of dilatation (v_{dil}).
 488

489 Additional sensitivity analyses, specifically on the effect of varying σ_n , T , d or d_{sb} , W_{sb} and
 490 W_{bulks} and ϕ_c and ϕ_0 (see Table 3 and Supplementary Text for their definition), consistently showed
 491 a τ - v curve characterized by a continuous transition from strong v -strengthening to -weakening
 492 behavior (Fig. 9). The critical velocity v_{cr} , which demarcates the transition in the sign of
 493 v -dependence, ranges from 0.1 to 0.7 micron/s within the range of parameter values tested.
 494 Specifically, an increase in (effective) normal stress (σ_n) results in a higher shear strength and an
 495 increase in v_{cr} . Increasing the temperature or decreasing the grain size (either d or d_{sb}) causes a

496 rightward horizontal translation of the τ - v curve implying a higher v_{cr} -value. Note that due to the
 497 limited thickness of the bulk gouge layer, the grain size (d_{bulk}) has a negligible effect on the shear
 498 strength. Lowering ϕ_c or increasing ϕ_0 does not change the τ - v profile but leads to a higher peak
 499 strength and more pronounced v -weakening in the frictional regime (i.e., for $v > v_{cr}$).

500 As already shown in Fig. 8, a decrease in W_{sb} causes a leftward horizontal translation of the
 501 τ - v curve (see also Fig. S5). Here we further investigated the effect of progressive localization,
 502 which may have occurred in the frictional regime at $v > v_{cr}$ that showed v -weakening (Beeler et al.,
 503 1996). To mimic this, we assumed a log-linear decrease in W_{sb} from 200 to 10 μm as v increases
 504 from the calculated v_{cr} to 1 mm/s. The predicted τ - v curve displays a higher v_{cr} and a deeper
 505 v -weakening at $v > v_c$ (Fig. 9D). This may explain why our reference simulation using a constant
 506 W_{sb} predicts a gentler v -weakening than observed in the experiment (see the comparison in Fig.
 507 S4).

508



509

510 Figure 9. Sensitivity of computed steady-state friction coefficient to variation in parameter values (σ_n , T ,
 511 d , ϕ_c and ϕ_0 , as well as progressively decreasing W_{sb}). Parametric analyses were performed for a wide
 512 range of slip rates from 0.001 $\mu\text{m/s}$ to 1000 $\mu\text{m/s}$, using two fault geometries (A, B for distributed shear,
 513 and C, D for localized slip). For both geometries, the reference cases (thick grey lines) employ the
 514 denoted parameter values and for each other curve we changed one parameter. All the definitions and
 515 values of the parameters are listed in Table 3.

516

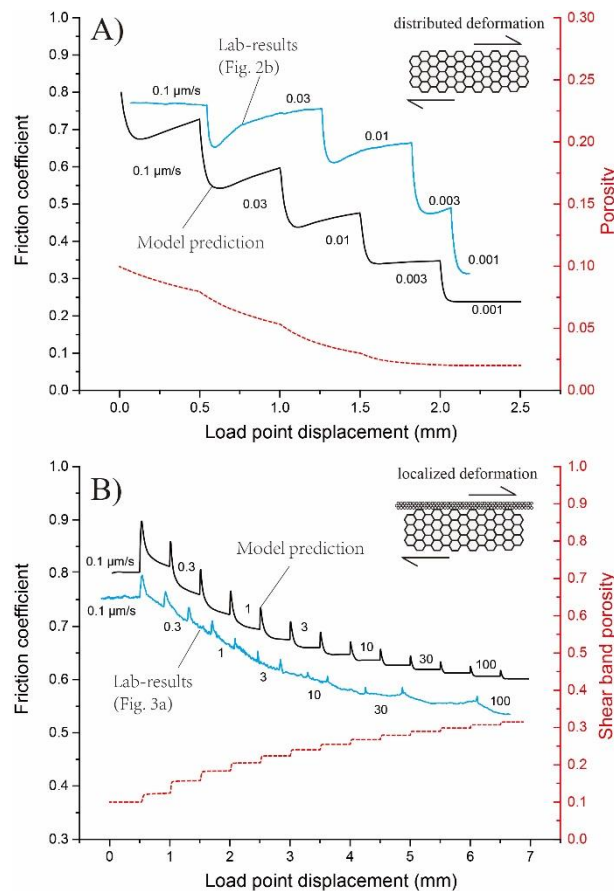
517 5.2.2. Simulation of Velocity Stepping Experiments

518 We next use the CNS model to investigate the transient shear deformation behavior, as
 519 observed in our v -stepping experiments. The experimental setup can be idealized as a spring-slider
 520 system (e.g. Chen & Spiers, 2016). From the initial response upon a perturbation in displacement
 521 rate, the apparent stiffness of the loading system measured 55 to 210 GPa/m. Taking a stiffness
 522 from this range, the model simulation will sometimes lead to stick-slips in the frictional regime,
 523 especially at relatively low velocities (e.g., for 0.3 $\mu\text{m/s} < v < 10 \mu\text{m/s}$), or when imposing a thin

524 shear band. Although the occurrence of stick-slip at low- v is consistent with the findings of
 525 Verberne et al. (2015), for calcite gouge sheared under the same T - σ_n - P_f conditions as used here, in
 526 the present experiments we consistently observed stable sliding. Therefore, in our model
 527 simulations we employed a stiffness of 500 GPa/m. Other model parameters are set to the same
 528 values as used for simulating steady state behavior (see Table 3). The initial displacement rate
 529 used in the model is set to 0.1 $\mu\text{m/s}$, beyond which we imposed the same v -stepping sequence as
 530 used in the experiments, allowing 0.5 mm of shear displacement in each v -interval. The initial
 531 shear stress and porosity were set according to the analytical expressions for steady state (Chen et
 532 al., 2017).

533 The model output alongside the experimental data are plotted as friction coefficient and
 534 porosity versus displacement in Fig. 10. For experiments conducted using $v < v_{cr}$, the predicted
 535 friction response shows a sharp drop followed by gradual restrengthening for the first three steps
 536 ($v \leq 0.01 \mu\text{m/s}$), comparing favorably with the experimental data (Fig. 10A). For each
 537 displacement rate tested, the model predicts continued compaction with increasing displacement.
 538 For $v \geq 0.003 \mu\text{m/s}$, when the porosity reaches the background level of φ_0 , the shear strength
 539 shows a monotonic decay, without re-strengthening. A plot of friction vs sample (or particle)
 540 velocity (i.e. $\mu - v_s$), termed a phase diagram by Gu et al. (1984), shows that the model simulation
 541 of downward v -steps defines a curve which is parallel to the interpolated experimental data (Fig.
 542 11), with a gap that decreases with increasing slip rate.

543



544

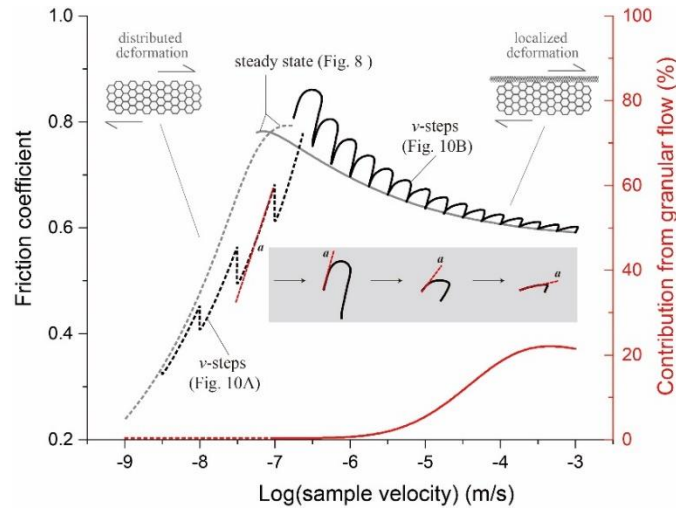
545 Figure 10. Predicted evolution of friction coefficient and porosity from the CNS model, to simulate A)
 546 the downward and B) upward v -stepping tests shown in Figs. 2 and 3, respectively. The experimental

547 data are added for comparison, with a slight extension of the x-axis for the comparing convenience.

548

549 The model output simulating the response in shear strength upon a step in displacement rate
 550 in v -stepping tests using $v > 0.1 \mu\text{m/s}$ is strikingly consistent with the experimental data (Fig. 10B
 551 and 11). Firstly, all simulated upward v -steps showed a classical, RSF-type, frictional response,
 552 constituting v -weakening. Secondly, when using the same magnitude v -steps (1.75-fold), the
 553 difference in μ_{ss} before and after a v -step becomes less as the post-step v increases, implying an
 554 increase of the steady-state frictional rate dependence (i.e., the $(a - b)$ value becomes less negative)
 555 with increasing v . Thirdly, the model output as well as the experimental data show a systematic
 556 decrease in the direct effect (i.e., the a -value) with increasing slip rate (see also the inset of Fig.
 557 11). The same trend also describes the characteristic slip distance (i.e., the D_c value). Lastly, for v
 558 $\leq 3 \mu\text{m/s}$, friction-displacement curves representing the model as well as the experimental data do
 559 not reach steady state within 0.5 mm of displacement, whereas for $v > 10 \mu\text{m/s}$ they do.

560



561

562 Figure 11. Friction-velocity phase diagram of the simulated v -steps shown in Fig. 10, with the
 563 predicted steady-state shear strength being added for comparison (in grey lines). Results from the
 564 friction and flow regimes, with distributed and localized deformation, are plotted in solid and dashed
 565 black lines, respectively. The red lines give the relative contribution from granular slip to the shear
 566 deformation. The grey inset illustrates the systematic decrease in the direct effect (or a -value) with
 567 increasing velocity.

568

569 The direct effect, defined as $a = d\mu/d(\ln v)$, can be directly measured as the slope of the
 570 instantaneous response in the μ - v_s phase diagram multiplied by $\ln(10)$ (see the inset of Fig. 11).
 571 We found that the direct effect continuously evolves from a flow-like process at low v to granular
 572 flow at high v . Specifically, for low velocity ($v < v_{cr}$), it measures as $a = a_{flow} = \mu/n$ where n is the
 573 stress exponent (eq. 2), while at high velocity ($v > v_{cr}$) its value gradually decreases from a_{flow} to
 574 $a_{\tilde{\mu}}$ which in the limit approaches the direct effect defined in in the RSF model (see Chen & Spiers,
 575 2016). To further specify this, we investigate the relative contribution to shear strain
 576 accommodation of plastic flow vs. granular flow, at steady state (see the red curves in Fig. 11). In
 577 the flow regime ($v < v_{cr}$), shear deformation is fully accommodated by plastic flow, except that
 578 created small increment of porosity starts to play a role at $v > v_{dil}$. As slip rate increases, granular

579 flow plays an increasingly important role, ultimately accounting for up to 22% of the total shear
 580 strain rate. Their relative contribution determines the a -value, that is $a = \eta a_{\dot{\mu}} + (1 - \eta) a_{flow}$, where
 581 $\eta = \dot{\gamma}_{gr} / (\dot{\gamma}_{gr} + \dot{\gamma}_{pl})$.

582

583 6. Discussion

584 6.1. Flow-to-Friction Transition and “Semi-brittle Flow” of Carbonates at 550 °C

585 In this study, we reported ring-shear experiments on layers of wet simulated calcite fault
 586 gouge sheared at 550 °C and 50 MPa effective normal stress conditions, at sliding velocities
 587 ranging from 0.001 to 300 $\mu\text{m/s}$. A plot of steady-state shear strength against sliding velocity (v)
 588 showed a transition with increasing v from v -strengthening to v -weakening, characterized by a
 589 peak shear strength at a critical velocity $v_{cr} = 0.1 \mu\text{m/s}$ (Fig. 4). Samples deformed at $v < 0.1 \mu\text{m/s}$
 590 are characterized by a dense, near-homogeneously deformed microstructure, compared with
 591 localized deformation in samples deformed at $v > 0.1 \mu\text{m/s}$. Our mechanical and microstructural
 592 findings are consistent with a transition with increasing slip rate from distributed, creep-controlled
 593 flow to localized, frictional slip beyond $v \approx 0.1 \mu\text{m/s}$. In the low- v flow regime, deformation is
 594 accommodated by compactive, plastic creep processes involving the entire width of the gouge
 595 layer. Towards higher slip rates ($v > 0.1 \mu\text{m/s}$), and in the case of localized slip, shear deformation
 596 by granular flow plays an increasingly important role. Despite the dramatic differences in the
 597 mechanical and microstructural characteristics between the ‘slow’ and the ‘fast’ shear deformation
 598 regimes, the creep mechanisms occurring between the grains may be modelled using an empirical
 599 constitutive law which represents a mixture of diffusion and dislocation creep.

600 The stress sensitivity or n -value determined for deformation in the flow regime showed an
 601 increase with increasing v , from 2.5 – 4.2 ($v \leq 0.01 \mu\text{m/s}$ or $\dot{\gamma} \leq 1.25 \times 10^{-6} \text{ s}^{-1}$) to 8.8 – 87 ($v \rightarrow$
 602 $0.1 \mu\text{m/s}$, or $\dot{\gamma} \rightarrow 1.25 \times 10^{-5} \text{ s}^{-1}$) (Fig. 7). An increase of the n -value from 2.1 to 4.2 with
 603 increasing strain rate was reported from compression tests on dense calcite aggregates at 500 –
 604 600 °C, by Bruhn et al. (1999). From the present post-mortem microstructures (Fig. 5, see also
 605 Verberne et al., 2017) and thickness measurements (Fig. S3), as well as the microphysical analysis
 606 of steady-state behavior (Fig. 8), we posit that the change in n -value (or slope in strain rate-stress
 607 curve) is caused by porosity development, or cavitation, at grain boundaries. Based on our
 608 microphysical model simulations (Fig. 8), intergranular cavitation is expected to become
 609 noticeable in the gouge shear mechanical properties when the sliding velocity overcomes the
 610 dilatancy velocity v_{dil} . With further increasing v , cavitation continues until the critical velocity v_{cr}
 611 is reached, which demarcates the flow-to-friction transition (Fig. 4) accompanied by the change
 612 from stable to unstable slip. Relatively high n -values and the development of porosity have also
 613 been observed in creep-type experiments on synthetic feldspar and granitoid rocks, conducted
 614 under conditions simulating the BDT (Rybacki et al., 2008; Delle Piane et al., 2009; Pec et al.,
 615 2016), and is often referred to as ‘semi-brittle flow’ behavior (Fredrich et al., 1989; Nicolas et al.,
 616 2017). “Semi-brittleness” can be verified by the emergence of normal stress dependence of shear
 617 strength, which shows that at a higher normal stress it is feasible to have continued deformation by
 618 purely plastic flow (without dilatancy) at elevated strain rates and therefore a higher v_{dil} -value
 619 (Figs. 9A and 9C).

620 In the semi-brittle shear deformation regime, the transient response to a sudden drop in
 621 loading velocity displays a sharp drop in shear stress followed by a gradual rise to a new steady
 622 state (Fig. 2). This is like that expected from a frictional response. Such transient behavior has

623 been observed in simulated halite(-mica) gouges sheared at room temperature and slow slip rates
624 (0.03 - 0.1 $\mu\text{m/s}$), as a precursor to a transition from v -strengthening to -weakening (Niemeijer &
625 Spiers, 2005). From our modelling results it appears as if deformation in the semi-brittle regime
626 remains fully plastic (i.e. > 99% contribution, Fig. 11), however, porosity development due to
627 cavitation effectively leads to local stress enhancement hence enhanced creep rates, at grain
628 contacts. In other words, the stress required to accommodate gouge shear deformation by dense
629 plastic flow, at zero or at least at very low porosity, is higher than that required to generate
630 porosity, and to advance deformation at elevated strain rates. This means that in the semi-brittle
631 deformation regime, it is energetically more favorable to create porosity than to sustain plastic
632 flow.

633

634 **6.2. Microphysical Modelling and Comparison with Previous Models**

635 Using constraints based on observed or measured properties of sheared calcite fault gouge,
636 the CNS model employed here predicts a flow-to-friction transition consistent with the
637 experimental data (Fig. 8). The CNS model distinguishes itself from previous constitutive models
638 describing fault deformation in the friction/flow regime such as the two-mechanism model
639 (Reinen et al., 1992; Chester, 1994; Estrin & Brechet, 1996; Nakatani, 2001; Beeler, 2009; Noda &
640 Shimamoto, 2010; Shimamoto & Noda, 2014), because it is based on lab-derived observations of
641 microphysical deformation processes.

642 From the point of view of fault rupture modelling, transient shear deformation behavior is
643 more important than steady-state, since the velocities vary greatly during earthquake ruptures and,
644 practically, a seismically-active fault is always in some transient stage of the earthquake cycle. We
645 have shown that the CNS model can favorably predict transient responses to v -steps in the friction
646 as well as the flow deformation regime (Figs. 10 and 11). In particular, the CNS model predicts
647 RSF-like behavior within the “semi-brittle flow” regime, which is consistent with that predicted
648 by the empirical model by Noda & Shimamoto (2010) who fitted a rate- and state-dependent flow
649 law to data from shear experiments on halite conducted at high temperatures. Finally, besides the
650 mechanical behavior, the CNS model predicts an increase in porosity with increasing slip rates
651 across the flow-to-friction transition (Fig. 10). Of interest is that the onset of dilatation occurs at a
652 velocity (v_{dil}) before the transition, which, as shall be discussed in the following, has important
653 implications for natural fault deformation at the BDT conditions.

654 Recently, Aharonov & Scholz (2018) developed a physics-based constitutive law for rock
655 friction, based on the microphysics of contact creep, using an exponential law, and the coupling
656 with frictional heating (hereafter referred to the A&S model). By considering the temperature and
657 stresses at asperities, which impact the direct rate dependence of friction (or a -value in the
658 framework of RSF theory) their model can lead to local (flash) melting, and predict different
659 deformation regimes as a function of slip rate. Significantly, the A&S model predictions are
660 essentially similar to those of the CNS model (Chen et al., 2017; Chen & Niemeijer, 2017). More
661 recently, Aharonov & Scholz (2019) have applied their model to higher temperature and pressure
662 conditions and showed that a brittle-to-ductile transition (BDT) with increasing depth is a direct
663 consequence of their model. The common foundation shared by the A&S and CNS models, is the
664 limit in net grain contact area, or porosity beyond which shear deformation switches from
665 creep-controlled flow to normal-stress dependent (or frictional) sliding. Thus, this porosity or
666 grain contact area limit is crucial for the conditions pertaining to the flow-to-friction transition

667 hence the depth to the BDT.

668

669 **6.3. Limitations and Future Work**

670 A potentially crucial uncertainty which we have not yet considered is to what extent
671 recrystallization (grain growth) occurred during or after shear deformation. As addressed in
672 section 4, the grains in the bulk gouges deformed at $v < 0.1 \mu\text{m/s}$ have likely grown with respect to
673 the starting material, in the early hours of the experiments. In the frictional regime ($v > 0.1 \mu\text{m/s}$)
674 one would expect a high porosity (c. 10 - 30%) in the active shear band due to the operation of
675 granular flow (Fig. 8). However, the post-mortem microstructure of the shear band occasionally
676 shows polygonal grains with straight boundaries and high-angle junctions, with a relatively low
677 porosity ($< 9\%$, Fig. 5C). We infer that the compacted structure could be developed by static
678 recrystallization in the termination stage of the experiments. Based on the observed grain size
679 distribution ($d = 0.3 - 1.4 \mu\text{m}$, with $\bar{d} \sim 0.8 \mu\text{m}$, Fig.5) and a temperature profile upon cooling
680 after the experiment (see supplement Fig. S6-A), we can estimate the maximum grain sizes prior
681 to annealing, using the grain growth equation for porous calcite aggregates (e.g., Covey-Crump,
682 1997). Assuming initial grain sizes from $0.01 \mu\text{m}$ to $1.0 \mu\text{m}$, the calculations predict that grain
683 growth mostly occurs within the first 50 s cooling (Fig. S6). For grains with an initial size (d_0)
684 smaller than $0.2 \mu\text{m}$, the final sizes after cooling are more or less constant and close to $\sim 0.45 \mu\text{m}$
685 (Fig. S6-B), whereas for grains with d_0 exceeding $0.2 \mu\text{m}$ the total growth in grain size is limited
686 to $0.25 \mu\text{m}$ (Fig. S6-C). The predicted minimum grain size of $0.45 \mu\text{m}$ is roughly consistent with
687 our final observation. Therefore, before terminating shearing, the shear bands may contain a
688 portion of grains that were smaller than the observation and have a systematically smaller mean
689 value (\bar{d}) by $\sim 0.15 \mu\text{m}$, with a small portion of grains ($\sim 10\%$) that could be smaller than 100 nm
690 (Fig. S6-D). This variation in the \bar{d} -value does fall in the range of our parametric analyses.
691 However, we cannot rule out that the dynamic grain size during active shear could be even smaller
692 (Verberbe et al., 2019). To explore this issue, experiments stopped at short shear displacements,
693 together with ad hoc quenching procedures, are required in the future.

694 From our experiments as well as the microphysical model it remains ambiguous as to how
695 semi-brittle flow, local porosity development, and/or slip instability leads to the formation of a
696 shear band (i.e., spontaneous slip localization and grain size reduction). We speculate that this
697 process may be tied to the development of dilatancy in the semi-brittle flow regime ($v_{dil} < v < v_{cr}$).
698 Rationalized from a microscopic point of view: cavities developed at grain boundaries will
699 generate high local stresses, which, added to the already high shear stress around the transition,
700 will cause grain breakage preferably at the cavitated points. As stress continues to build up and
701 more cavities develop, a previously creeping gouge can readily dilate from these cavities, leading
702 to the emergence of strain localization and therefore the incipience of a shear band. In other words,
703 it is the inability of semi-brittle flow to maintain the contiguity of a creeping gouge layer that
704 leads to local disaggregation and thus the formation of shear band. Previous laboratory and
705 numerical modelling studies also showed, in general, that shear localization occurs due to the
706 presence of local heterogeneities, such as those in porosity and grain size distribution (Hadizadeh
707 et al., 2010, 2015; Nübel & Huang, 2004), which could potentially lead to the ductile-to-brittle
708 transition. Of course, a continuous flow-to-friction transition, together with the associated
709 microstructural evolution (i.e., localization and grain size reduction), occurs spontaneously in both
710 laboratory and natural shear zones (Platt & Behr, 2011; Wehrens et al., 2017), which is not yet

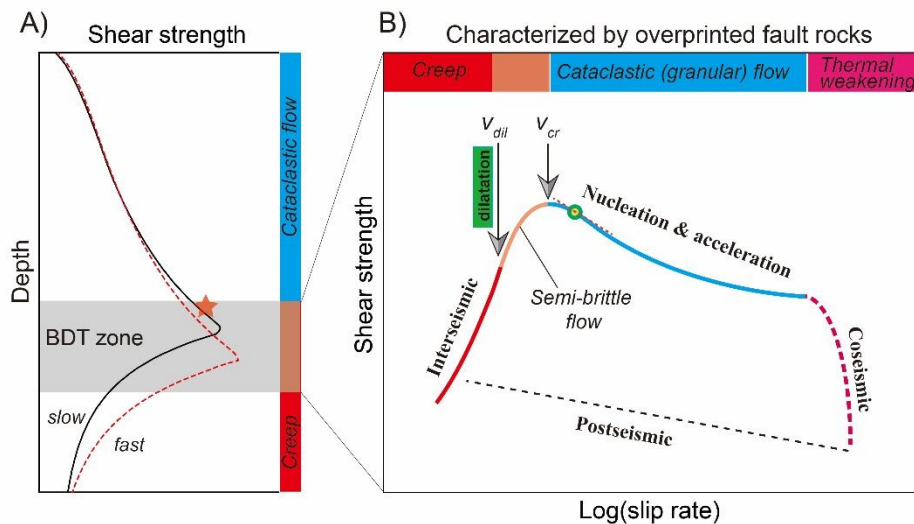
711 captured by the present model and will be considered in future work.

712

713 6.4. Implications for Fault Rupture Dynamics within the BDT Zone

714 Based on the present experimental and microphysical modelling results we sketch a diagram
 715 showing the shear strength-depth profile of a carbonate fault (Fig. 12A), with the expected fault
 716 rupture dynamics in the brittle-to-ductile transition (BDT) zone (Fig. 12B). For simplicity, the
 717 change of shear strength with increasing depth was predicted using the same model (i.e., the case
 718 of localized slip), but taking two constant loading velocities (10^{-10} and 10^{-9} m/s) and a geotherm of
 719 $25^\circ\text{C}/\text{km}$.

720 At shallow depths, the shear strength shows a near-linear increase with increasing depth,
 721 representing frictional behavior (Fig. 12A). The difference between slow and fast loading
 722 velocities indicates a transition from v -strengthening to v -weakening with increasing depth. As
 723 depth increase, the peak strength on the profile marks the friction-to-flow transition (Fig. 12A). As
 724 embodied in the CNS model, this transition depth depends not only on the loading velocity but
 725 also on fault zone structure such as grain size and shear zone thickness, as well as fault conditions
 726 such as the thermal and effective pressure gradients. The variation of this transition depth,
 727 resulting from a range of velocities which the fault could potentially experience in an earthquake
 728 cycle, then defines the width of the BDT zone (see the grey zone in Fig. 12A).



729

730 Figure 12. Diagrams illustrating (A) the shear strength-depth profile of a carbonate fault zone over the
 731 crustal depth at fast and slow velocities, and (B) the strength-velocity profile showing the dynamic of
 732 an earthquake that nucleates within the brittle-ductile transition (BDT) zone.

733

734 When an earthquake nucleates from a fault patch (or asperity) at the base of the seismogenic
 735 zone (see the red star in Fig. 12A), which is usually considered to be the upper bound of the BDT
 736 zone, it is expected that the fault patch will undergo a transition from stable, ductile flow over a
 737 wide shear zone, to unstable, localized frictional slip by cataclastic (granular) flow, involving a
 738 wide range of slip rates (see the thick line in Fig. 12B). Before the transition, the fault will first
 739 show semi-brittle flow behavior accompanied by the onset of dilatation as described in the earlier
 740 sections. Besides the evidence from laboratory experiments, similar mechanical and
 741 microstructural characteristics have also been observed in ductile fault rocks collected from

742 natural shear zones exhumed from the aseismic/seismic transition depths (25 - 35 km,
 743 Regenauer-Lieb, 1999; Shigematsu et al., 2004; Fousseis & Handy, 2008; Fousseis et al., 2009;
 744 Menegon et al., 2015; Platt et al., 2018; Gilgannon et al., 2017), sometimes using different
 745 terminologies such as “ductile rupture”, “dilatant plasticity”, “dilatant microcracking” and “creep
 746 cavitation”. Our microphysical modelling predicts that “semi-brittle flow” occurs over a velocity
 747 range from the onset of dilatation until the transition to friction ($v_{dil} < v < v_{cr}$). An important
 748 implication is that the mechanical and microstructural features can be taken as indicators of the
 749 (aseismic) acceleration stage for a seismogenic fault to produce an instability at higher slip rates.

750 As the fault accelerates and continues to dilate at $v > v_{cr}$, its shear strength decreases, and an
 751 earthquake nucleates. However, as the fault just transitions into the v -weakening regime, the initial
 752 minimum nucleation size will be rather large since $(a - b)$ has only a small negative value.
 753 However, as the fault accelerates further, $(a - b)$ becomes more negative and this size will shrink
 754 until it reaches its minimum size at the steepest point in Fig. 12B, indicated by the red circle. As
 755 the slip area increases beyond the critical nucleation size, the rupture propagates and runaway slip
 756 occurs (Scholz, 2002). Finally, as the slip runs away to the coseismic regime (~ 1 m/s), some
 757 thermal weakening mechanisms such as flash heating will start to play a role (Niemeijer et al.,
 758 2012, Di Toro et al., 2011), leading to dramatic weakening. For a fault cutting carbonate rocks,
 759 one of the candidate mechanisms is grain boundary sliding with accommodation by diffusion
 760 creep (De Paola et al., 2015). Implementing this mechanism to explain carbonate dynamic
 761 weakening is a natural extension of the present model (i.e., simply using different creep law and
 762 with high temperature generated by frictional heating) and is in progress.

763 Finally, as discussed above, within the BDT zone the deformation and failure modes might
 764 switch between ductile non-localized plastic flow and brittle-localized patterns within the
 765 timeframe of earthquake cycles. The resultant fault rocks will be characterized by repeated
 766 overprinting of different deformation processes, specifically interseismic mylonitization,
 767 subseismic cataclasis and localization, and coseismic melting or superplasticity. These include
 768 pseudotachylyte overprinted with mylonitic deformation, mylonitized cataclasite, and cataclasite
 769 containing mylonite clasts (e.g., Takagi et al., 2000; Fousseis et al., 2009; Frost et al., 2011;
 770 Fagereng, 2011; Wehrens et al., 2016, 2017; Wintsch & Yeh, 2013). It is noteworthy that what is
 771 more commonly seen in outcrops are different layers of fault rocks coexisting across the fault zone
 772 (mylonite, cataclasite, pseudotachylyte, and fault gouge), which might form separately in different
 773 scenarios (e.g., along with the exhumation of the fault toward the surface).

774

775 7. Conclusions

776 In this study, we performed constant-velocity and velocity-stepping tests on layers of
 777 simulated calcite fault gouge at 550 °C, 50 MPa effective normal stress, and 100 MPa fluid
 778 pressure conditions, with slip rates covering almost six orders of magnitude (0.001 – 300 $\mu\text{m/s}$).
 779 The shear strength observed at these velocities shows a flow-to-friction transition within
 780 increasing slip rates, with a critical velocity (v_{cr}) of 0.1 $\mu\text{m/s}$.

781 Distinct microstructures were displayed in the two regimes. In the flow regime ($v < 0.1$ $\mu\text{m/s}$),
 782 the gouge is well compacted, displaying a progressive homogeneous texture as slip rate decreases,
 783 while in the frictional regime ($v \geq 0.1$ $\mu\text{m/s}$), a localized shear band was developed. A stress
 784 sensitivity with approximate n -values of 2.5 – 8.8 was recognized for the flow regime, which, in
 785 combination with the characteristic microstructure (i.e. compacted, polygonal grains with high

786 junction angles, some with subtle elongation), and CPO pattern observed, suggests deformation by
 787 a mixture of dislocation and diffusion creep. The same creep mechanism was inferred to also
 788 occur in the friction regime but is expected to accommodate only a part of the shear deformation,
 789 with the rest accommodated by granular flow which generates porosity and in turn enhances local
 790 stress and creep rate.

791 Incorporating the microstructures and inferred creep mechanisms, the microphysical model
 792 (CNS model) reproduces the steady-state shear strength profile showing the transition from flow
 793 to friction with increasing slip rate, as well as the transient flow/friction behavior in the
 794 flow/friction regime. In the frictional regime ($v > v_{cr}$), the model predicts typical v -weakening
 795 behavior; as velocity increases, there is a systematic decrease in the absolute value of $(a - b)$, the
 796 a - and D_c - values, as velocity increases. The flow regime can be divided into two sub-regimes,
 797 separating from a velocity for the onset of dilatation (v_{dil}). At $v < v_{dil}$, the fault deforms by pure
 798 plastic flow following a power law, while at $v > v_{dil}$, the fault deforms by “semi-brittle flow”,
 799 characterized by high stress sensitivity and a transient behavior similar to the RSF frictional
 800 behavior. All the predictions are generally consistent with the observations from experiments.

801 Implications for the dynamics of earthquake ruptures at the brittle-to-ductile transition zone
 802 are made based on the results from present experiments and microphysical model. In particular,
 803 our results show that the “semi-brittle flow” is occurring at velocities ranging from v_{dil} to v_{cr} and is
 804 linked to the opening of transient micro-porosity (or cavitation). As applied to a natural carbonate
 805 fault zone, the characteristics of the “semi-brittle” flow behavior sheds considerable insights for
 806 earthquake nucleation at the base of the seismogenic zone, i.e. as indicators of a precursory phase.

807

808 Acknowledgements

809 We thank Tony van der Gon-Netscher, Ing. Floris van Oort, and Gert Kastelein for technical
 810 support, and Yongmei Shang and Xi Ma for assisting with the EBSD analyses. We thank Prof.
 811 Chris Spiers and Prof. Hans De Bresser for discussions. This project is funded by the European
 812 Research Council, grant SEISMIC (335915), and by the Dutch Research Council, VIDI grant
 813 (854.12.011), awarded to ARN. BAV was supported by JSPS KAKENHI grant #19K14823.
 814 Experimental raw data and microphysical models with input data are all freely available through:
 815 <https://doi.org/10.4121/uuid:63a7dbde-e223-43ad-b184-bc7f111f883c>.

816

817 Reference

- 818 1. Aharonov, E., & Scholz, C. H. (2018). A physics-based rock friction constitutive law: Steady
 819 state friction. *Journal of Geophysical Research*, 123, 1591–1614.
- 820 2. Aharonov, E., & Scholz, C. H. (2019). The brittle-ductile transition predicted by a physics -
 821 based friction law. *JGR*, 124, 2721–2737.
- 822 3. Blanpied, M. L., Lockner, D. A., & Byerlee, J. D. (1995). Frictional slip of granite at
 823 hydrothermal conditions. *Journal of Geophysical*
 824 *Research*, 100(B7), 13,045 – 13,064.
- 825 5. Beeler, N.M. (2009). Constructing constitutive relationships for seismic and aseismic fault
 826 slip, *Pure and Applied geophysics*, 166, 1775–1798.
- 827 6. Bestmann, M., Pennacchioni, G., Nielsen, S., Göken, M., & de Wall H. (2012). Deformation
 828 and ultrafine dynamic recrystallization of quartz in pseudotachylyte-bearing brittle faults: A
 829 matter of a few seconds. *J. Struct. Geol.*, 38, 21-38.

- 830 7. Bos, B., & Spiers, C. J. (2002). Fluid-assisted healing processes in gouge bearing faults:
831 Insights from experiments on a rock analogue system. *Pure and Applied Geophysics*, 159,
832 2537–2566.
- 833 8. Brace, W. F., & Kohlstedt, D. L. (1980). Limits on lithospheric stress imposed by laboratory
834 experiments. *Journal of Geophysical Research*, 85(B11), 6248–6252.
- 835 9. Brantut, N., Heap, M. J., Meredith, P. G. & Baud, P. (2013). Time dependent cracking and
836 brittle creep in crustal rocks: A review. *J. Struct. Geol.*, 52, 17–43.
- 837 10. Bruhn, D. F., Olgaard, D. L., & Dell'Angelo, L. N. (1999). Evidence of enhanced
838 deformation in two-phase rocks: Experiments on the rheology of calcite-anhydrite aggregates.
839 *Journal of Geophysical Research*, 104, 707–724.
- 840 11. Chen, J., & Spiers, C. J. (2016). Rate and state frictional and healing behavior of carbonate
841 fault gouge explained using microphysical model. *Journal of Geophysical Research*, 121,
842 8642–8665.
- 843 12. Chen, J., & Niemeijer, A. R. (2017). Seismogenic potential of a gouge-filled fault and the
844 criterion for its slip stability: Constraints from a microphysical model. *Journal of*
845 *Geophysical Research*, 122, 9658–9688.
- 846 13. Chen, J., Niemeijer, A. R., & Spiers, C. J. (2017). Microphysically derived expressions for
847 rate - and - state friction parameters, a , b , and D_c . *Journal of Geophysical Research*, 122,
848 9627–9657.
- 849 14. Chen, J., van den Ende, M. P. A., & Niemeijer, A. R. (2020). Microphysical model
850 predictions of fault restrengthening under room - humidity and hydrothermal conditions:
851 From logarithmic to power - law healing. *Journal of Geophysical Research*, 125,
852 e2019JB018567. <https://doi.org/10.1029/2019JB018567>
- 853 15. Chester, F. M. (1988). The brittle-ductile transition in a deformation-mechanism map for
854 halite. *Tectonophysics*, 154, 125–136.
- 855 16. Chester, F. M. (1994). Effects of temperature on friction: Constitutive equations and
856 experiments with quartz gouge. *Journal of Geophysical Research*, 99(B4), 7247–7261.
- 857 17. Chester, F. M., & Higgs, N. G. (1992). Multimechanism friction constitutive model for
858 ultrafine quartz gouge at hypocentral conditions. *JGR: Solid Earth*, 97(B2), 1859-1870.
- 859 18. Covey-Crump, S. J. (1997). The normal grain growth behaviour of nominally pure calcite
860 aggregates. *Contrib. Mineral. Petrol.* 129, 239–254.
- 861 19. De Bresser, J. H. P., Evans, B. & Renner, J. (2002). On estimating the strength of calcite
862 rocks under natural conditions. *Geol. Soc. London Spec. Pub.* 200, 309–329.
- 863 20. De Paola, N., Holdsworth, R.E., Viti, C., Colletini, C., & Bullock, R. (2015). Can grain size
864 sensitive flow lubricate faults during the initial stages of earthquake propagation?. *Earth and*
865 *Planetary Science Letters*, 431, 48–58.
- 866 21. Delle Piane, C., Wilson, C. J. L. & Burlini L. (2009). Dilatant plasticity in high-strain
867 experiments on calcite - muscovite aggregates. *J. Struct. Geol.*, 31(10), 1084–1099,
868 doi:10.1016/j.jsg.2009.03.005.
- 869 22. Den Hartog, S. A. M., Niemeijer, A. R., & Spiers, C. J. (2013). Friction on subduction
870 megathrust faults: Beyond the illite - muscovite transition. *Earth and Planetary Science*
871 *Letters*, 373, 8–19.
- 872 23. Di Toro, G., Han, R., Hirose, T., De Paola, N., Nielsen, S., Mizoguchi, K., Ferri, F., Cocco,
873 M., & Shimamoto T. (2011). Fault lubrication during earthquakes. *Nature*, 471, 493–499.

- 874 24. Drury, M. R., Humphreys, F. J. & White, S. H. (1985). Large strain deformation studies
875 using polycrystalline magnesium as a rock analogue. Part II: dynamic recrystallisation
876 mechanisms at high temperatures. *Phys. Earth Plan. Int.*, 40, 208-222.
- 877 25. Estrin, Y. & Brechet, Y. (1996). On a model of frictional sliding. *Pure Appl. Geophys.*, 4,
878 745–762.
- 879 26. Fagereng, A. (2011). Geology of the seismogenic subduction thrust interface. Geological
880 Society, London, Special Publications 359, 55-76.
- 881 27. Fredrich, J. T., Evans, B., Wong, T.-F. (1989). Micromechanics of the brittle to plastic
882 transition in Carrara marble. *J. Geophys. Res.*, 94, 4129 - 4145
- 883 28. Frost, E., Dolan, J., Ratschbacher, L., Hacker, B., & Seward, G. (2011). Direct observation of
884 fault zone structure at the brittle-ductile transition along the
885 Salzach-Ennstal-Mariazell-Puchberg fault system, Austrian Alps. *J. Geophys. Res.*, 116,
886 B02411, doi:10.1029/2010JB007719.
- 887 29. Fousseis, F., & Handy, M.R. (2008). Micromechanisms of shear zone propagation at the
888 brittle-viscous transition. *J. Struct. Geol.* 30, 1242-1253.
- 889 30. Fousseis, F., Regenauer-Lieb, K., Liu, J., Hough, R. M. & De Carlo, F. (2009). Creep
890 cavitation can establish a dynamic granular fluid pump in ductile shear zones. *Nature* 459,
891 974–977.
- 892 31. Gifkins, R. C. (1970). *Optical microscopy of metals*, Elsevier, New York.
- 893 32. Gilgannon, J., Fousseis, F., Menegon, L., Regenauer-Lieb, K., & Buckman, J. (2017).
894 Hierarchical creep cavity formation in an ultramylonite and implications for phase mixing.
895 *Solid Earth*, 85194, 1193–1209.
- 896 33. Gu, J. C., Rice, J. R., Ruina, A. L., & Tse, S. T. (1984). Slip motion and stability of a single
897 degree of freedom elastic system with rate and state dependent friction. *Journal of the*
898 *Mechanics and Physics of Solids*, 32, 167–196.
- 899 34. Hadizadeh, J., Sehhati, R., & Tullis, T. (2010). Porosity and particle shape changes leading to
900 shear localization in small-displacement faults. *J. Struct. Geol.*, 32, 712-720.
- 901 35. Hadizadeh, J., Tullis, T., White, J. C., & Konkachbaev, A. I. (2015). Shear localization,
902 velocity weakening behavior, and development of cataclastic foliation in experimental
903 granite gouge. *Journal of Structural Geology*, 71, 86-99.
- 904 36. Hayman, N. W., & Lavier, L. L. (2014). The geologic record of deep episodic tremor and slip.
905 *Geology* 42 (3), 195–198.
- 906 37. Herwegh, M., Xiao, X., & Evans, B. (2003). The effect of dissolved magnesium on diffusion
907 creep in calcite. *Earth Planet. Sci. Lett.* 212, 457-470.
- 908 38. Holdsworth, R. E., Stewart, M., Imber, J. & Strachan, R. A. (2001). The structure and
909 rheological evolution of reactivated continental shear zones: a review and case study. *Geol.*
910 *Soc. London Spec. Publ.* 184, 115–137.
- 911 39. Imber, J., Holdsworth, R. E., Smith, S. A. F., Jefferies, S. P. & Collettini, C. (2008).
912 Frictional-viscous flow, seismicity and the geology of weak faults: a review and future
913 directions. *Geol. Soc. London Spec. Publ.* 299, 151–173.
- 914 40. Jiang, J., & Lapusta, N. (2016). Deeper penetration of large earthquakes on seismically
915 quiescent faults. *Science*, 352(6291), 1293–1297.
- 916 41. Kawamoto, E., & Shimamoto, T. (1997). Mechanical behavior of halite and calcite shear
917 zones from brittle to fully-plastic deformation and a revised fault model, in *Proceedings of*

- 918 the 30th International Geological Congress, Beijing, China, 4–14 August 1996, vol. 14, pp.
919 89–105.3, VSP, Utrecht, Netherlands.
- 920 42. Lafrance, B., White, J. C., & Williams, P. F. (1994). Natural calcite c-axis fabrics: An
921 alternate interpretation. *Tectonophysics*, 229, 1–18.
- 922 43. Meissner, R., & Strehlau, J. (1982). Limits of stresses in continental crusts and their relation
923 to the depth-frequency distribution of shallow earthquakes. *Tectonics*, 1, 73–89.
- 924 44. Menegon, L., Fusses, F., Stunitz, H., & Xiao, X. (2015). Creep cavitation bands control
925 porosity and fluid flow in lower crustal shear zones. *Geology* 43, 227–230.
- 926 45. Nakatani, M. (2001). Conceptual and physical clarification of rate and state friction:
927 Frictional sliding as a thermally activated rheology. *Journal of Geophysical Research*,
928 106(B7), 13,347–13,380.
- 929 46. Nicolas, A., Fortin, J., Regnet, J. B., Verberne, B. A., Plümper, O., Dimanov, A., Spiers, C. J.,
930 & Guéguen, Y. (2017). Brittle and semibrittle creep of Tavel limestone deformed at room
931 temperature. *J. Geophys. Res.*, 122, 4436–4459.
- 932 47. Niemeijer, A. R. & Spiers, C. J. (2005). Influence of phyllosilicates on fault strength in the
933 brittle-ductile transition: Insights from rock analogue experiments. In “High Strain Zones:
934 Structure and Physical Properties”, D. Bruhn and L. Burlini (eds) Special Publication.
935 Geological Society of London, pp. 303-327.
- 936 48. Niemeijer, A. R., & Spiers, C. J. (2006). Velocity dependence of strength and healing
937 behaviour in simulated phyllosilicate-bearing fault gouge. *J. Geophys. Res.*, 427, 231–253.
- 938 49. Niemeijer, A. R., & Spiers, C. J. (2007). A microphysical model for strong velocity
939 weakening in phyllosilicate - bearing fault gouges. *Journal of Geophysical Research*, 112,
940 B10405. <https://doi.org/10.1029/2007JB005008>
- 941 50. Niemeijer, A. R., Spiers, C. J., & Peach, C. J. (2008). Frictional behavior of simulated quartz
942 fault gouges under hydrothermal conditions: Results from ultra-high strain rotary shear
943 experiments. *Tectonophysics* 460, 288-303.
- 944 51. Niemeijer, A., Di Toro, G., Smith, S. A. F., Griffith, A. W., Bistacchi, A., & Nielsen S.
945 (2012). Inferring earthquake physics and chemistry using an integrated field and laboratory
946 approach. *J. Struct. Geol.*, 39, 2–36.
- 947 52. Niemeijer, A. R., Boulton, C., Toy, V. G., Townend, J., & Sutherland, R. (2016).
948 Large-displacement, hydrothermal frictional properties of DFDP-1 fault rocks, Alpine Fault,
949 New Zealand: Implications for deep rupture propagation, *J. Geophys. Res.*, 121, 624–647.
- 950 53. Niemeijer A. R. (2018). Velocity-dependent slip weakening by the combined operation of
951 pressure solution and foliation development. *Scientific Reports*, 8: 4724,
952 DOI:10.1038/s41598-018-22889-3.
- 953 54. Noda, H., & Shimamoto, T. (2010). A rate- and state-dependent ductile flow law of
954 polycrystalline halite under large shear strain and implications for transition to brittle
955 deformation, *Geophys. Res. Lett.*, 37, L09310, doi:10.1029/2010GL042512.
- 956 55. Nübel, K., & Huang, W. (2004). A study of localized deformation pattern in granular media.
957 *Comput. Method Appl. M.*, 193, 2719-2743.
- 958 56. Pec, M., Stunitz, H., Heilbronner, R., & Drury, M. (2016). Semi-brittle flow of granitoid fault
959 rocks in experiments. *J. Geophys. Res.*, 121, 1677–1705.
- 960 57. Platt, J. P., & Behr, W. M. (2011). Grain size evolution in ductile shear zones: Implications
961 for strain localization and the strength of the lithosphere. *J. Struct. Geo.*, 33, 537 – 550.

- 962 58. Platt, J. P., Xia, H., & Schmidt, W. L. (2018). Rheology and stress in subduction zones
963 around the aseismic/seismic transition. *Progress in Earth and Planetary Science*, 5: 24,
964 <https://doi.org/10.1186/s40645-018-0183-8>.
- 965 59. Prior, D. J., Boyle, A. P., Brenker, F., Cheadle, M. C., Day, A., Lopez, G., Purezzo, L., Potts,
966 G. J., Reddy, S., Spiess, R., Timms, N. E., Trimby, P.W., Wheeler, J., & Zetterstrom, L.
967 (1999). The application of electron backscatter diffraction and orientation contrast imaging in
968 the SEM to textural problems in rocks. *American Mineralogist* 84, 1741-1759.
- 969 60. Regenauer-Lieb, K. (1999). Dilatant plasticity applied to Alpine collision: ductile void
970 growth in the intraplate area beneath the Eifel volcanic field. *Geodynamics* 27, 1–21.
- 971 61. Reinen, L. A., Tullis, T. E. & Weeks, J. D. (1992). Two-mechanism model for frictional
972 sliding of serpentinite. *Geophys. Res. Lett.*, 19(15), 1535–1538.
- 973 62. Rutter, E. H., Casey, M., & Burlini, L. (1994). Preferred crystallographic orientation
974 development during the plastic and superplastic flow of calcite rocks. *J. Struct. Geol.*, 16,
975 1431–1446.
- 976 63. Rybacki, E., Wirth, R. & Dresen, G. (2008). High-strain creep of feldspar rocks; implications
977 for cavitation and ductile failure in the lower crust. *Geophys. Res. Lett.* 35, L04304.
- 978 64. Schmid, S. M., Boland, J. N. & Paterson, M. S. (1977). Superplastic flow in finegrained
979 limestone. *Tectonophysics*, 43, 257–291.
- 980 65. Schmid, S. M., Panozzo, R. & Bauer, S. (1987). Simple shear experiments on calcite rocks;
981 theology and microfabric. *Journal of Structural Geology*, 9, 747-778.
- 982 66. Schmid, S. M., Paterson, M. S. & Boland, J. N. (1980). High temperature flow and dynamic
983 recrystallization in Carrara Marble. *Tectonophysics*, 65, 245- 280.
- 984 67. Scholz, C.H. (1988). The brittle-plastic transition and the depth of seismic faulting. *Geol.*
985 *Rundsch.*, 77, 319–328.
- 986 68. Scholz, C. H. (2002). *The mechanics of earthquakes and faulting* (2nd edition). Cambridge:
987 Cambridge University Press.
- 988 69. Shigematsu, N., Fujimoto, K., Ohtani, T. & Goto, K (2004). Ductile fracture of fine-grained
989 plagioclase in the brittle-plastic transition regime: implication for earthquake source
990 nucleation. *Earth Planet. Sci. Lett.* 222, 1007–1022.
- 991 70. Shimamoto, T. (1986). Transition between frictional slip and ductile flow for halite shear
992 zones at room temperature. *Science* 231, 711–714.
- 993 71. Shimamoto, T., & Noda, H. (2014). A friction to flow constitutive law and its application to a
994 2-D modelling of earthquakes, *J. Geophys. Res.*, 119, 8089–8106.
- 995 72. Sibson, R.H. (2003). Thickness of the seismic slip zone. *Bull. Seismol. Soc. Am.*, 93, 1169–
996 1178.
- 997 73. Stipp, M., Stünitz, H., Heilbronner, R., & Schmid, S. M. (2002). The Eastern Tonale fault
998 zone: A “natural laboratory” for crystal plastic deformation of quartz over a temperature
999 range from 250°C to 700°C. *J. Struct. Geol.*, 24, 1861–1884.
- 1000 74. Takagi, H., Goto, K. & Shigematsu, N. (2000). Ultramytonite bands derived from cataclastite
1001 and pseudotachylite in granites, northeast Japan. *J. Struct. Geol.* 22, 1325–1339.
- 1002 75. Takahashi, M., van den Ende, M. P. A., Niemeijer, A. R., & Spiers, C. J. (2017). Shear
1003 localization in a mature mylonitic rock analog during fast slip. *Geochem. Geophys. Geosyst.*,
1004 18, doi:10.1002/2016GC006687

- 1005 76. Tse, S. T., & Rice, J. R. (1986). Crustal earthquake instability in relation to the depth
1006 variation
1007 of frictional slip properties. *J. Geophys. Res.* 91 (B9), 9452.
- 1008 Ueda, T., Obata, M., Di Toro, G., Kanagawa, K., & Ozawa, K. (2008). Mantle earthquakes
1009 frozen in mylonitized ultramafic pseudotachylytes of spinel - lherzolite facies. *Geology*,
1010 36(8), 607 – 610. <https://doi.org/10.1130/G24739A.1>
- 1011 77. Verberne, B. A., Niemeijer, A. R., De Bresser, J. H. P., & Spiers, C.J. (2015). Mechanical
1012 behavior and microstructure of simulated calcite fault gouge sheared at 20–600 °C:
1013 Implications for natural faults in limestones. *J. Geophys. Res.*, 120, 8169–8196.
- 1014 78. Verberne, B. A., Chen, J., Niemeijer, A. R., de Bresser, J. H. P., Pennock, G. M., Drury, M.
1015 R., & Spiers, C. J. (2017). Microscale cavitation as a mechanism for nucleating earthquakes
1016 at the base of the seismogenic zone. *Nat. Commun.*, 8, 1645.
- 1017 79. Verberne, B. A., Plümpner O., & Spiers, C. J. (2019). Nanocrystalline principal slip zones and
1018 their role in controlling crustal fault rheology. *Minerals*, 9, 328, doi:10.3390/min9060328
- 1019 80. Vermeer, P.A., & De Borst, R. (1984). Non-associated plasticity for soils, concrete and rock.
1020 *HERON* 29 (3).
- 1021 81. Walker, A. N., Rutter, E. H. & Brodie, K. H. (1990). Experimental study of grain-size
1022 sensitive flow of synthetic, hot-pressed calcite rocks, in *Deformation Mechanisms, Rheology*
1023 *and Tectonics*, edited by R. J. Knipe and E. H. Rutter, *Geol. Soc. Spec. Publ.*, 54, 259-284.
- 1024 82. Wehrens, P., Baumberger, R., Berger, A., & Herwegh, M. (2017). How is strain localized in
1025 a meta-granitoid, mid-crustal basement section? Spatial distribution of deformation in the
1026 central Aar massif (Switzerland). *J. Struct. Geol.*, 94, 47-67.
- 1027 83. Wehrens, P., Berger, A., Herwegh, M., Peters, M., & Spillmann, T. (2016). Deformation at
1028 the frictional-viscous transition: evidence for cycles of fluid-assisted embrittlement and
1029 ductile deformation in the granitoid crust. *Tectonophysics*, 693, 66 – 84.
- 1030 84. Wintsch, R. P., & Yeh, M. W. (2013). Oscillating brittle and viscous behavior through the
1031 earthquake cycle in the Red River Shear Zone: Monitoring flips between reaction and
1032 textural softening and hardening. *Tectonophysics*, 587, 46-62.

Table 1. Experiments and Related Key Parameters ^a.

run	v ($\mu\text{m/s}$)	μ_{max}	x_{max} (mm)	μ_{ss}	$\Delta\mu_r$	x_{ss} (mm)	x_{final} (mm)
u513	300	0.99	0.74	0.365	0.007	4.1 - 7.4	7.4
u550-fast ^b	100	1.04	0.52	0.482	0.004	5.0 - 9.0	10.3
u603	30	1.07	1.10	0.588	0.010	5.0 - 7.3	7.3
u635	10	1.02	0.95	0.602	0.011	5.0 - 7.2	7.2
u550-slow ^b	10	0.91	0.70	0.548	0.002	4.0 - 5.2	5.2
u594	3.0	0.93	0.80	0.673	0.005	7.5 - 10.2	10.2
u507	1.0	0.83	0.55	0.634	0.011	5.0 - 7.3	7.3
u593	0.3	0.95	0.60	0.716	0.019	5.0 - 7.1	7.1
u516	0.1	1.02	0.90	0.802	0.002	5.0 - 7.8	7.8
u508	0.027	0.83	1.50	0.806	0.015	3.5 - 5.6	5.6
u499 ^c	1.0	0.84	0.45	0.625	0.006	3.5 - 5.4	10.7
continued by	1.0 \rightarrow 0.54 \rightarrow 0.3 \rightarrow 1.0 \rightarrow 0.30 \rightarrow 0.1 \rightarrow 1.0 \rightarrow 3.0 \rightarrow 10 \rightarrow 54 \rightarrow 100 $\mu\text{m/s}$						
μ_{ss}	0.625 0.603 0.610 0.601 0.613 0.630 0.613 0.563 0.516 0.476 0.427						
u502 ^c	0.1	0.83	1.42	0.761	0.005	5.0 - 7.2	22.0
continued by	0.1 \rightarrow 0.175 \rightarrow 0.3 \rightarrow 0.54 \rightarrow 1 \rightarrow 1.75 \rightarrow 3 \rightarrow 5.4 \rightarrow 10 \rightarrow 17.5 \rightarrow 30 \rightarrow 54 \rightarrow 100 \rightarrow 175 \rightarrow 300 $\mu\text{m/s}$						
μ_{ss}	0.761 0.742 0.715 0.691 0.664 0.644 0.624 0.608 0.588 0.577 0.568 0.554 0.488 0.522 0.520						
u517 ^c	0.1	1.02	0.90	0.807	0.015	4.2 - 7.2	7.8
continued by	0.1 \rightarrow 0.01 $\mu\text{m/s}$						
μ_{ss}	0.807 0.700						
u597 ^c	0.1	1.00	1.60	0.759	0.041	4.0 - 6.2	8.6
continued by	0.1 \rightarrow 0.03 \rightarrow 0.01 \rightarrow 0.003 $\mu\text{m/s}$						
μ_{ss}	0.759 0.766 0.764 0.549						
u605 ^c	0.1	0.90	1.30	0.782	0.004	5.0 - 6.0	8.5
continued by	0.1 \rightarrow 0.03 \rightarrow 0.01 \rightarrow 0.003 \rightarrow 0.001 $\mu\text{m/s}$						
μ_{ss}	0.782 0.762 0.672 0.500 0.338						

^a. v = imposed shear velocity, μ_{ss} = steady-state friction coefficient, $\Delta\mu_r$ = standard deviation of the μ_{ss} measured, x_{ss} = the shear displacement (x) range used to measure the steady-state friction, μ_{max} = maximum (or apparent yield) friction coefficient, x_{max} = the x -position to measure the peak friction, and x_{final} = final shear displacement.

^b. Results derived from the experiments performed by Verberne et al. (2017) under the same conditions.

^c. Stable sliding at $v = 0.1 \mu\text{m/s}$ was followed by v -steps, for which the μ_{ss} and $\Delta\mu_r$ values are displayed in Fig. 4.

Table 2. Proposed Constitutive Creep Laws of Calcite at High Temperature-Pressure Conditions ^a

	$\log A$ ($s^{-1}\mu m^{-m}MPa^{-n}$)	E_a (kJ/mol)	n	m	Source
GSS	6.68	213	1.70	3.00	Schmid et al.(1977): regime 3
GSS	7.63	200	1.10	3.26	Herwegh et al. (2003)
GSS + GSI	2.00	190	3.33	1.34	Walker et al. (1990): intermediate σ/T
GSI	3.10	420	7.60	-	Schmid et al. (1980): regime 2
GSI	8.10	428	4.20	-	Schmid et al. (1980): regime 3
GSI	16.65	584	-	-	De Bresser (2002)

^a GSS and GSI denote grain-size sensitive and grain-size insensitive creep, respectively. The constitutive creep laws proposed are either in a power form $\dot{\epsilon} = A \exp\left(-\frac{E_a}{RT}\right) \frac{\sigma^n}{d^m}$ or an exponential form $\dot{\epsilon} = A \exp\left(-\frac{E_a}{RT}\right) \exp\left(\frac{\sigma}{B}\right)$, where T , σ and d are in units of K, MPa, and μm , respectively. The factor B is 2.43 MPa in the exponential law proposed by De Bresser (2002).

Table 3. Microphysical Model Parameters and Values

Symbol	Description (unit)	Values ^a	Source
σ_n	effective normal stress	50 MPa	Present experiment
T	temperature	550 °C	Present experiment
K	stiffness of a simulated fault	6×10^{11} Pa/m	This study
W	thickness of the homogeneous gouge layer	0.8 mm	Microstructure
d	nominal grain size of a homogeneous gouge layer	3 (2 – 4) μm	Microstructure
W_{sb}	shear band thickness in the case of localized slip	50 (30 – 100) μm	Microstructure
W_{bulk}	thickness of the bulk zone in the case of localized slip	0.8 mm- W_{sb}	Microstructure
d^{sb}	nominal grain size of the shear band	0.8 μm	Microstructure
d^{bulk}	grain size in the bulk layer	5.0 μm	Microstructure
φ_c	critical state porosity for granular flow	0.4	This study
φ_0	terminal porosity of a compacted gouge	0.02	Chen & Niemeijer (2017)
φ_{ini}	Initial porosity in both shear and bulk layer	0.10	This study
p	sensitivity parameter in porosity function	2.0	Spiers et al. (2004)
H	geometrical parameter for grain package	0.57	Chen & Spiers (2016)
$\tilde{\mu}^*$	grain boundary (gb) friction coefficient at 1 $\mu m/s$	0.45	This study
$\tilde{\mu}$	logarithmic rate dependence of gb friction	0.01	Chen & Niemeijer (2017)

^a Values in the brackets give the variations for parametric analysis. Constant parameter values in the creep law are given in Table 2 (GSS + GSI, Walker et al., 1990).

Figure 1.

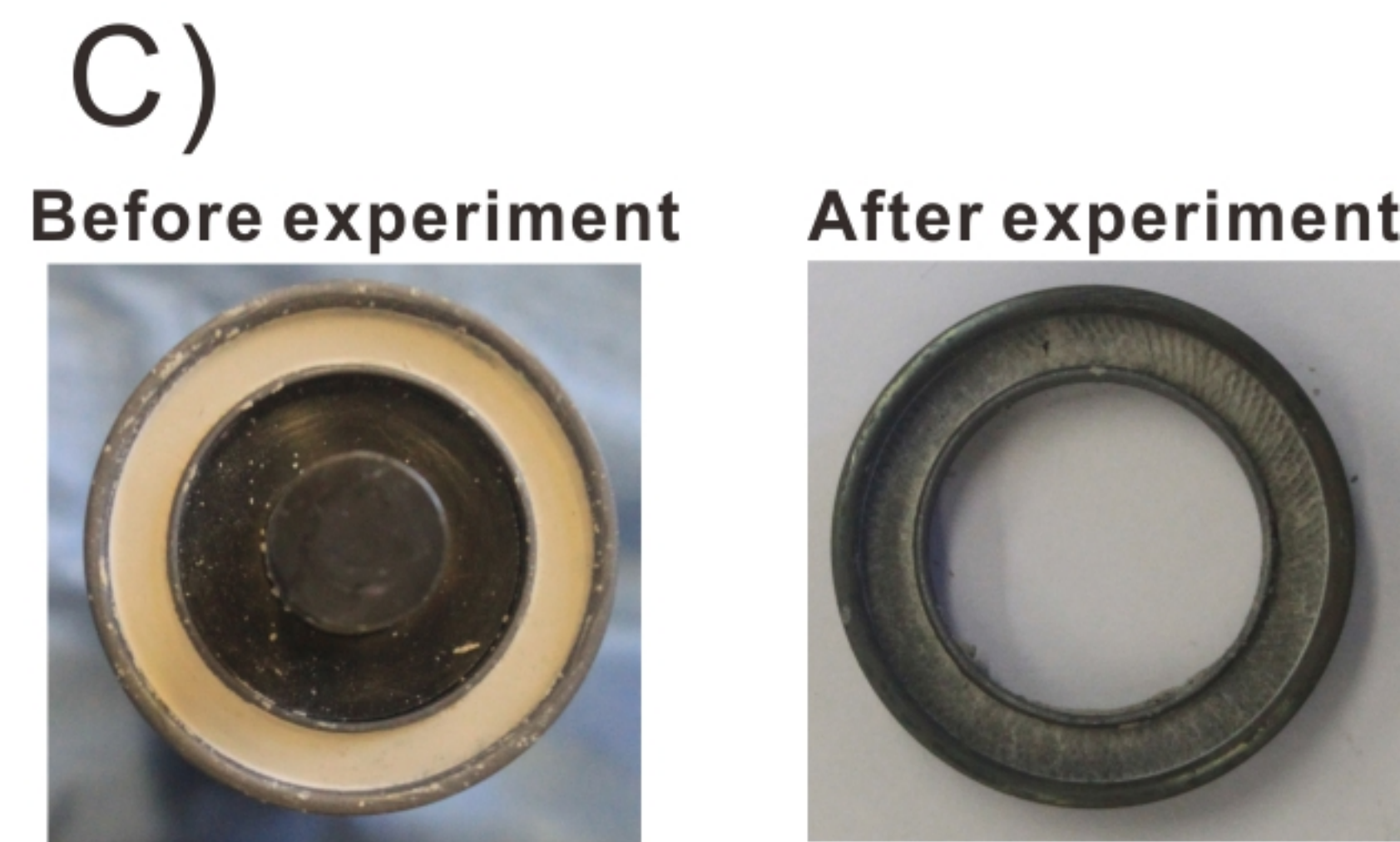
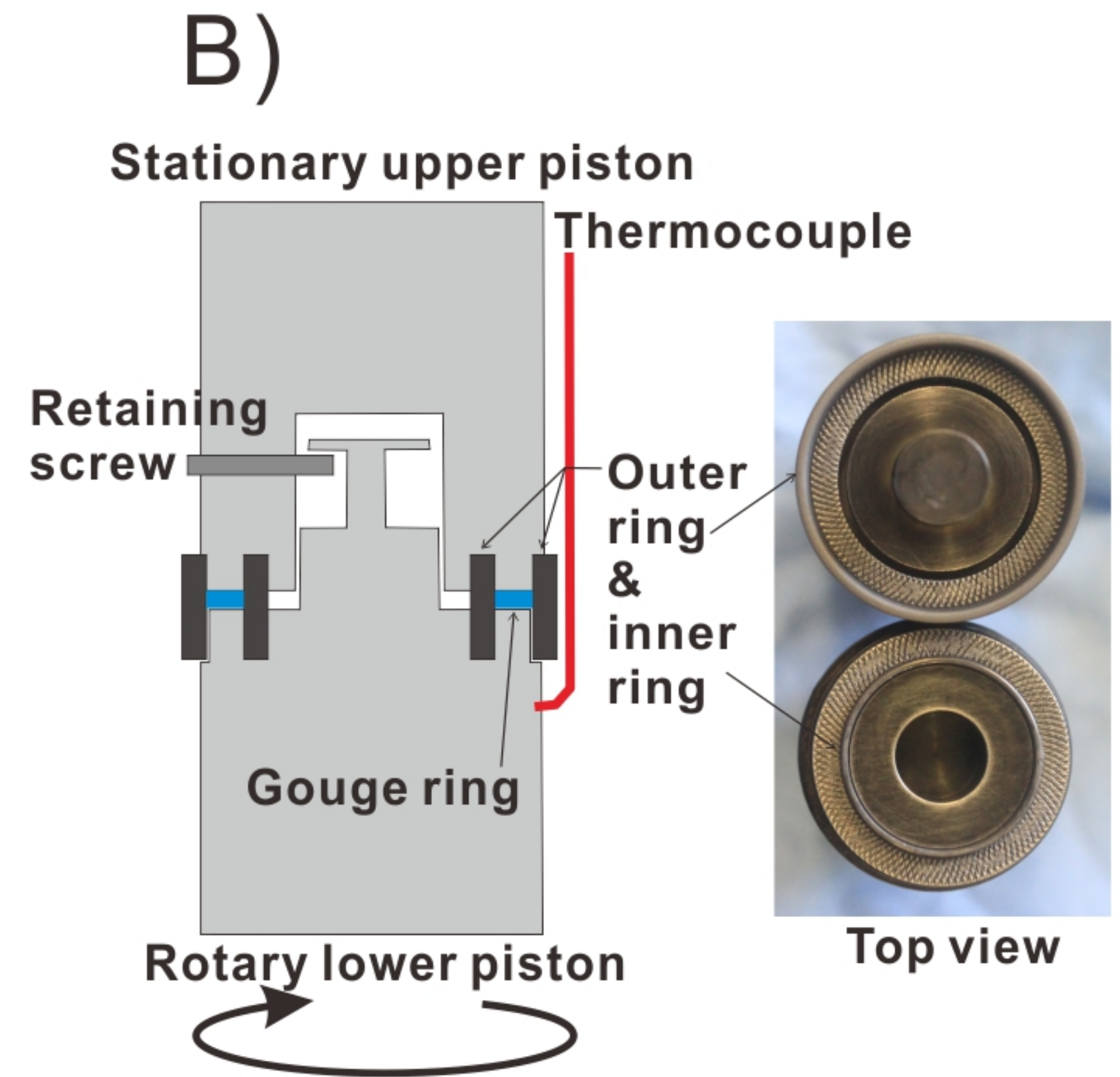
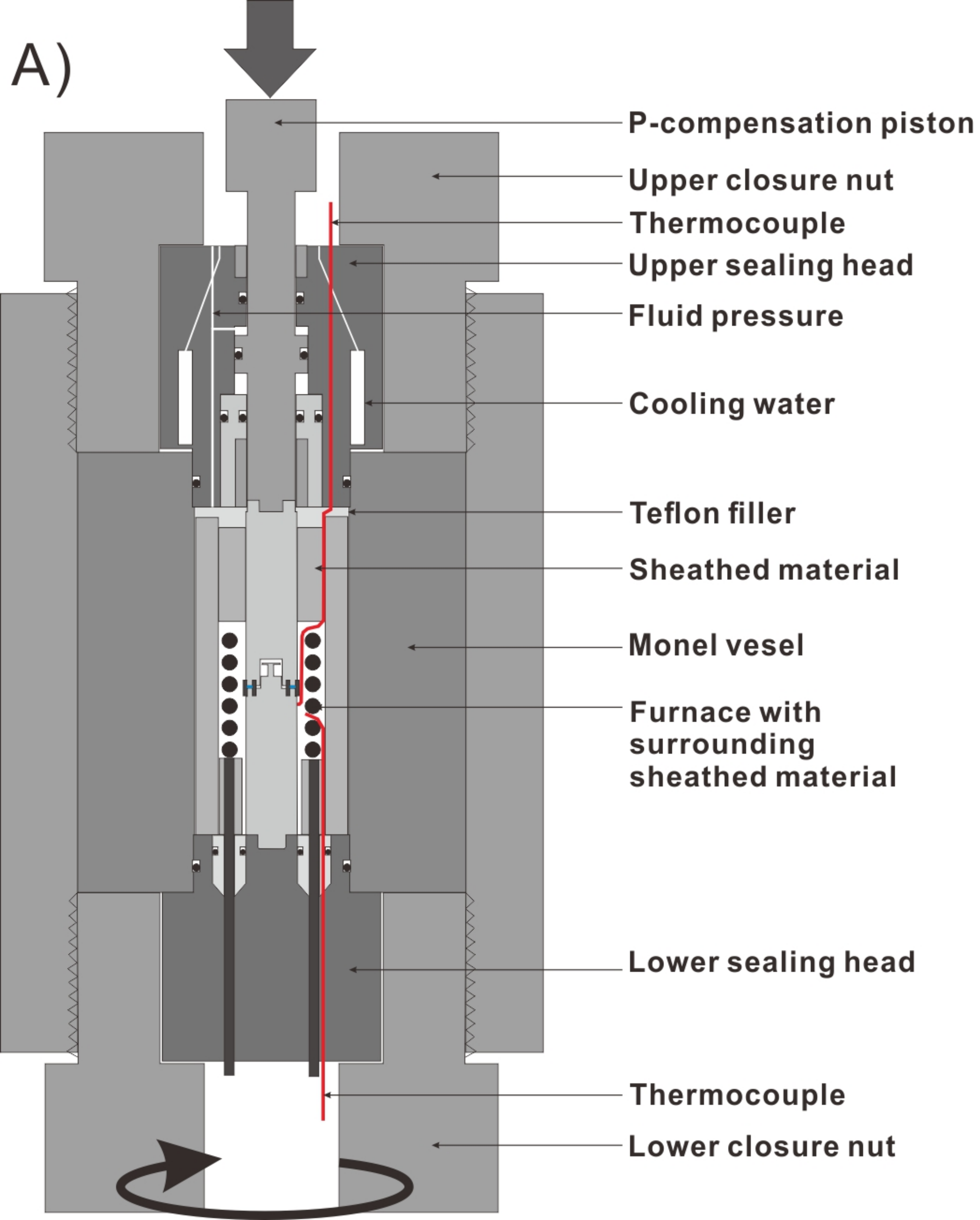


Figure 2.

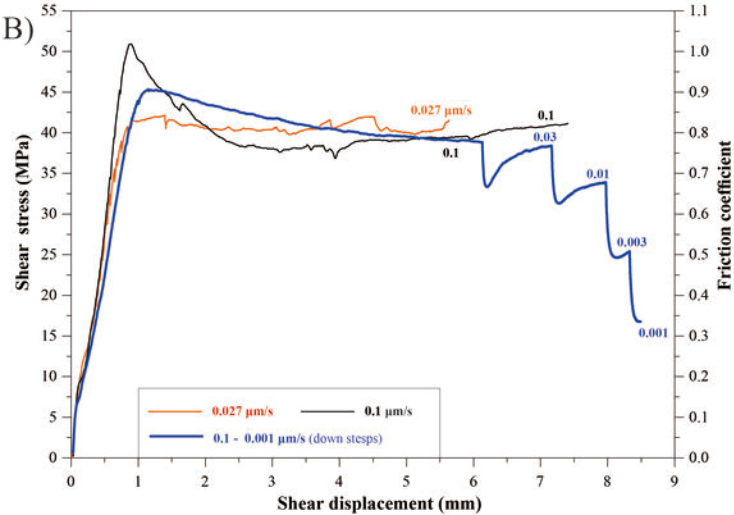
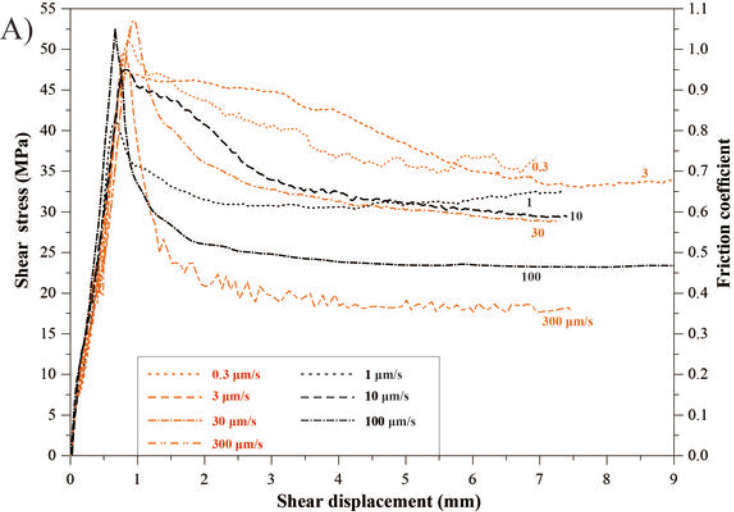


Figure 3.

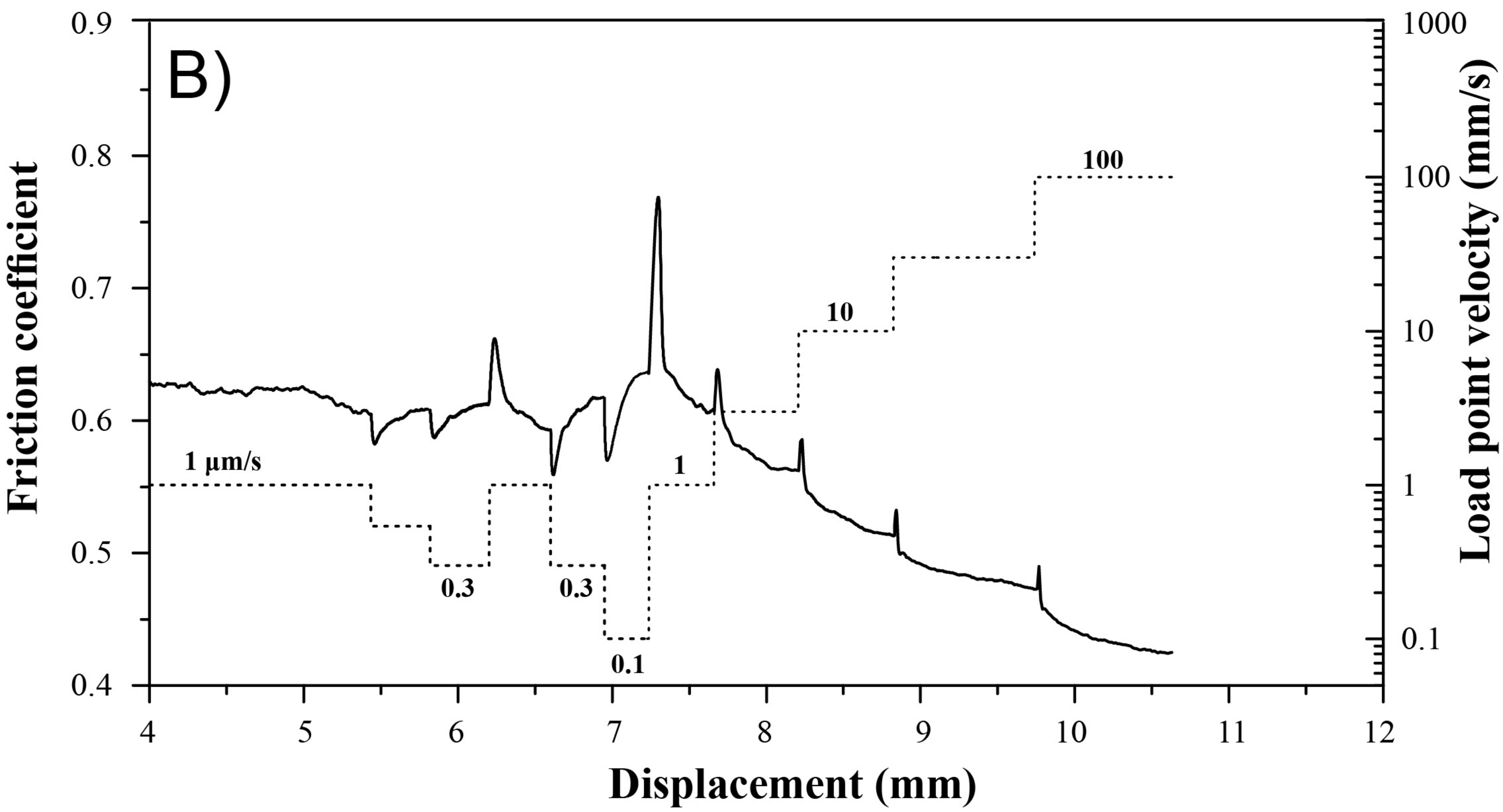
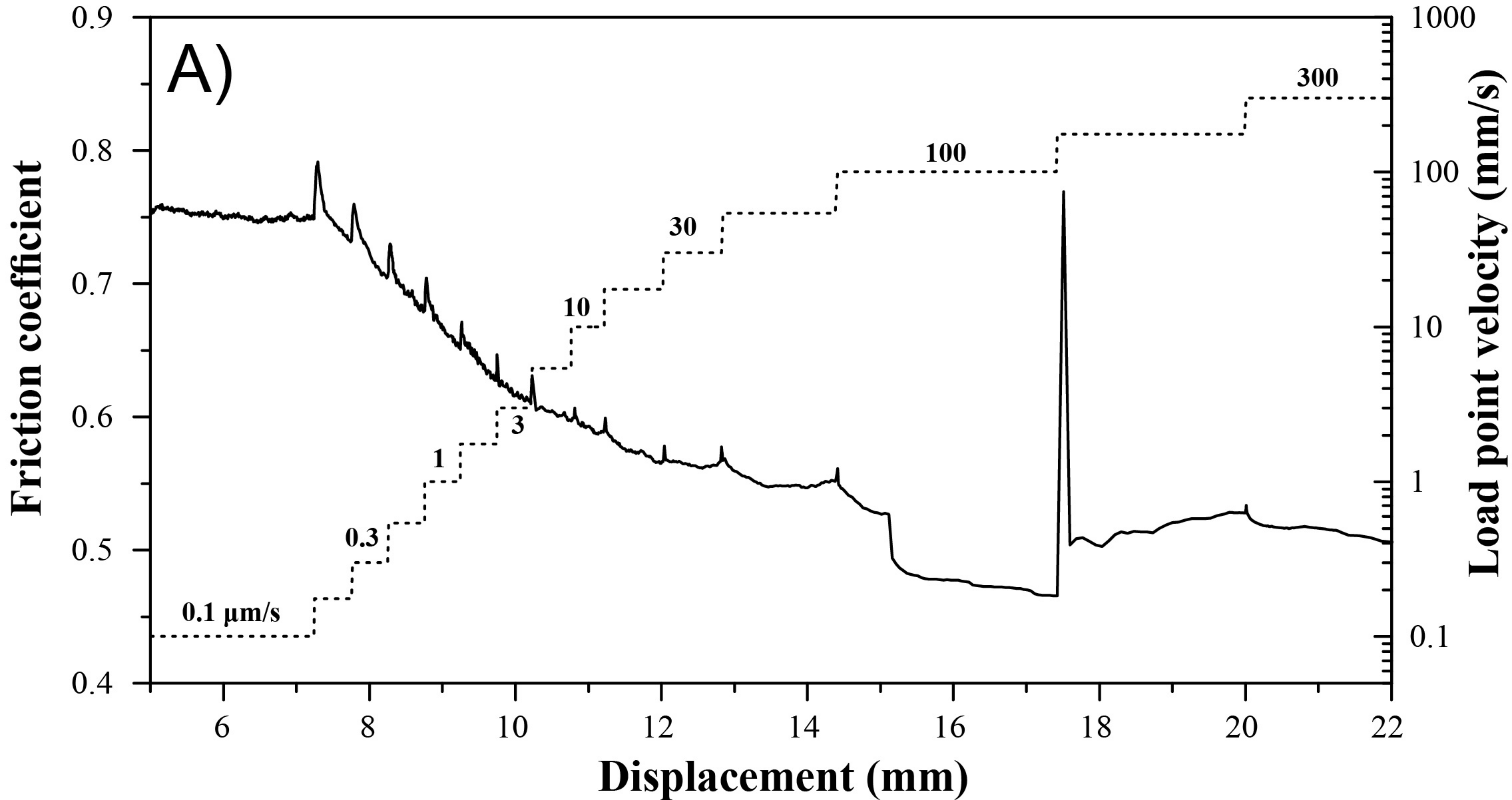


Figure 4.

Figure 5.

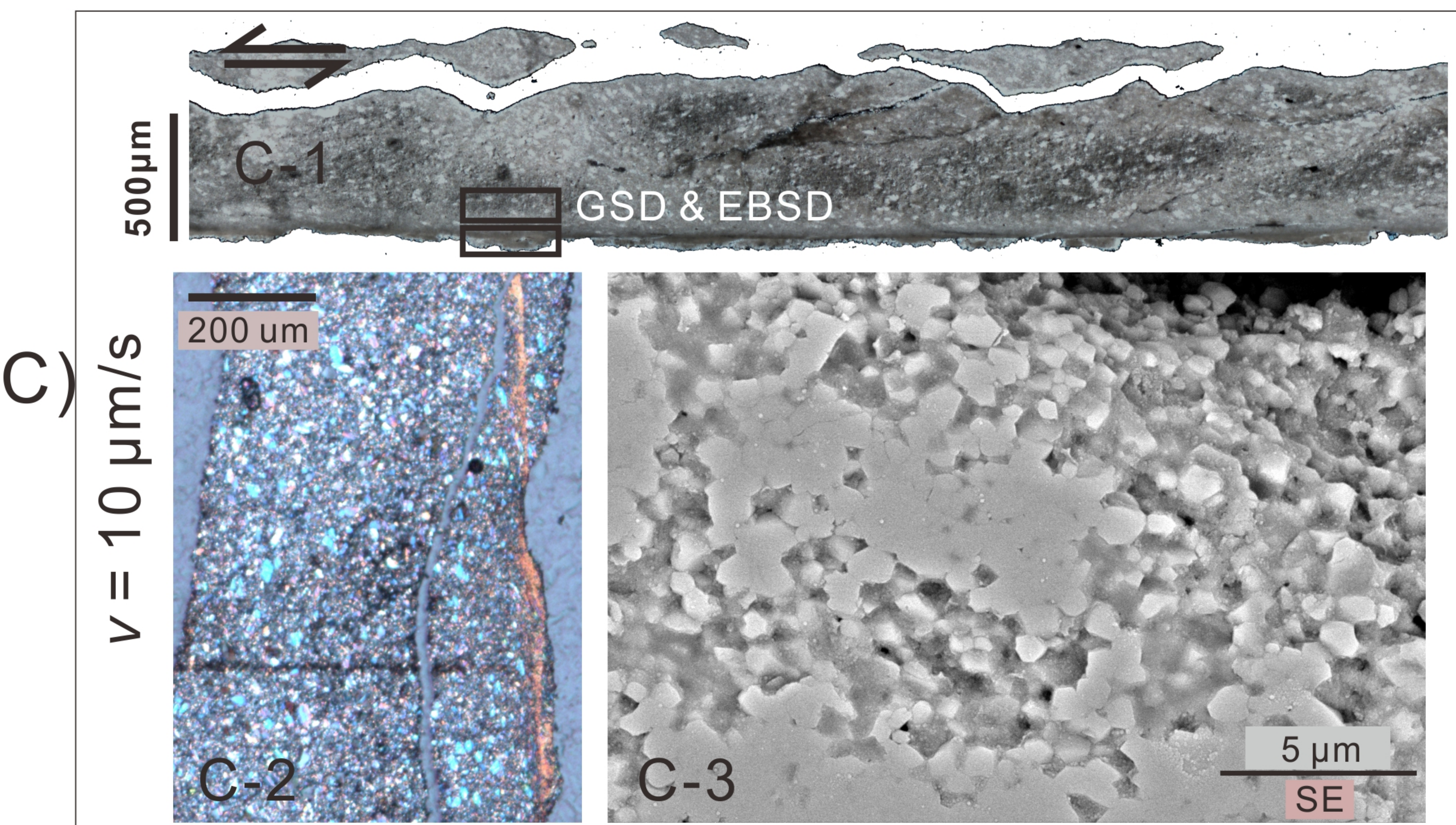
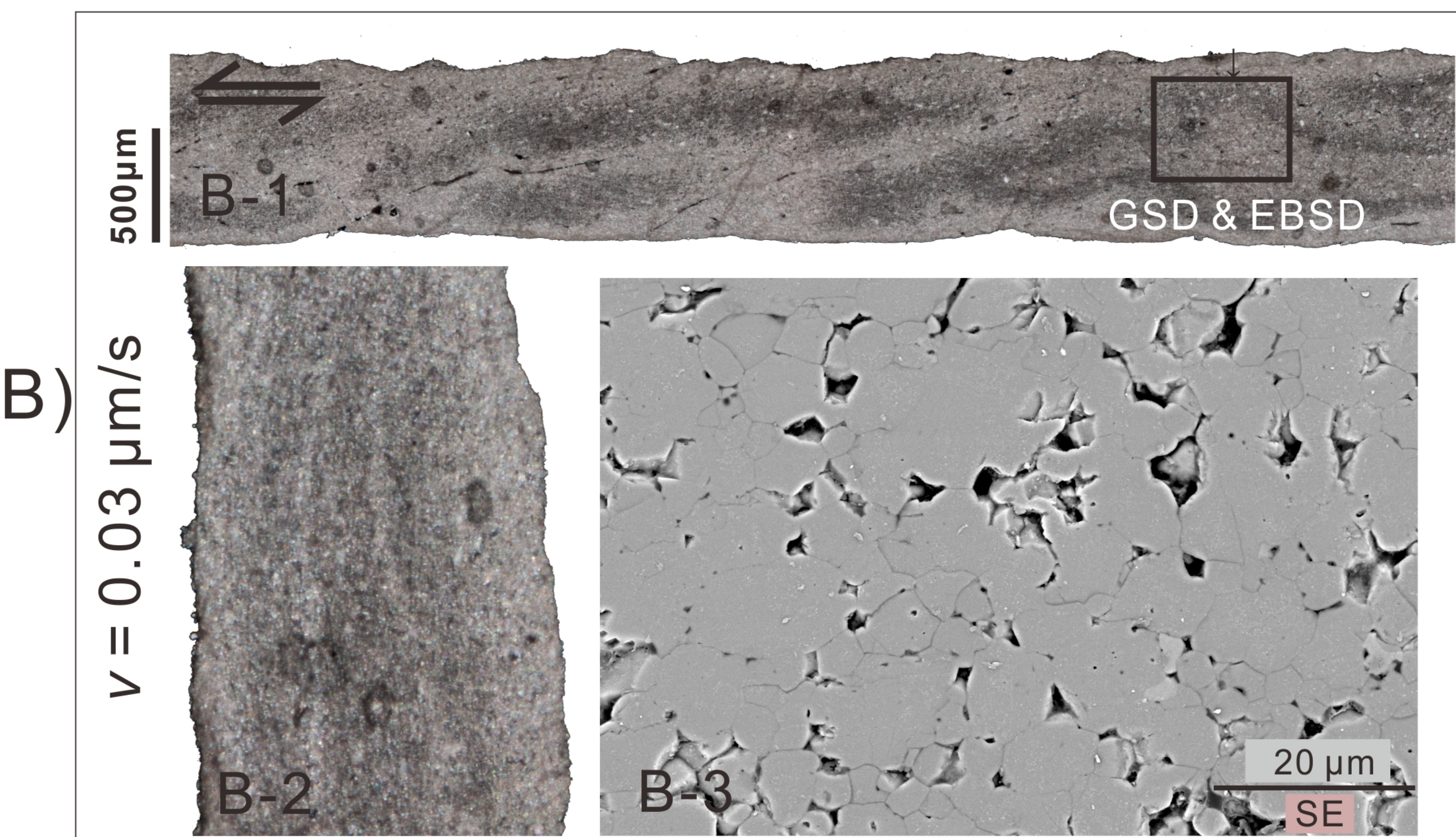
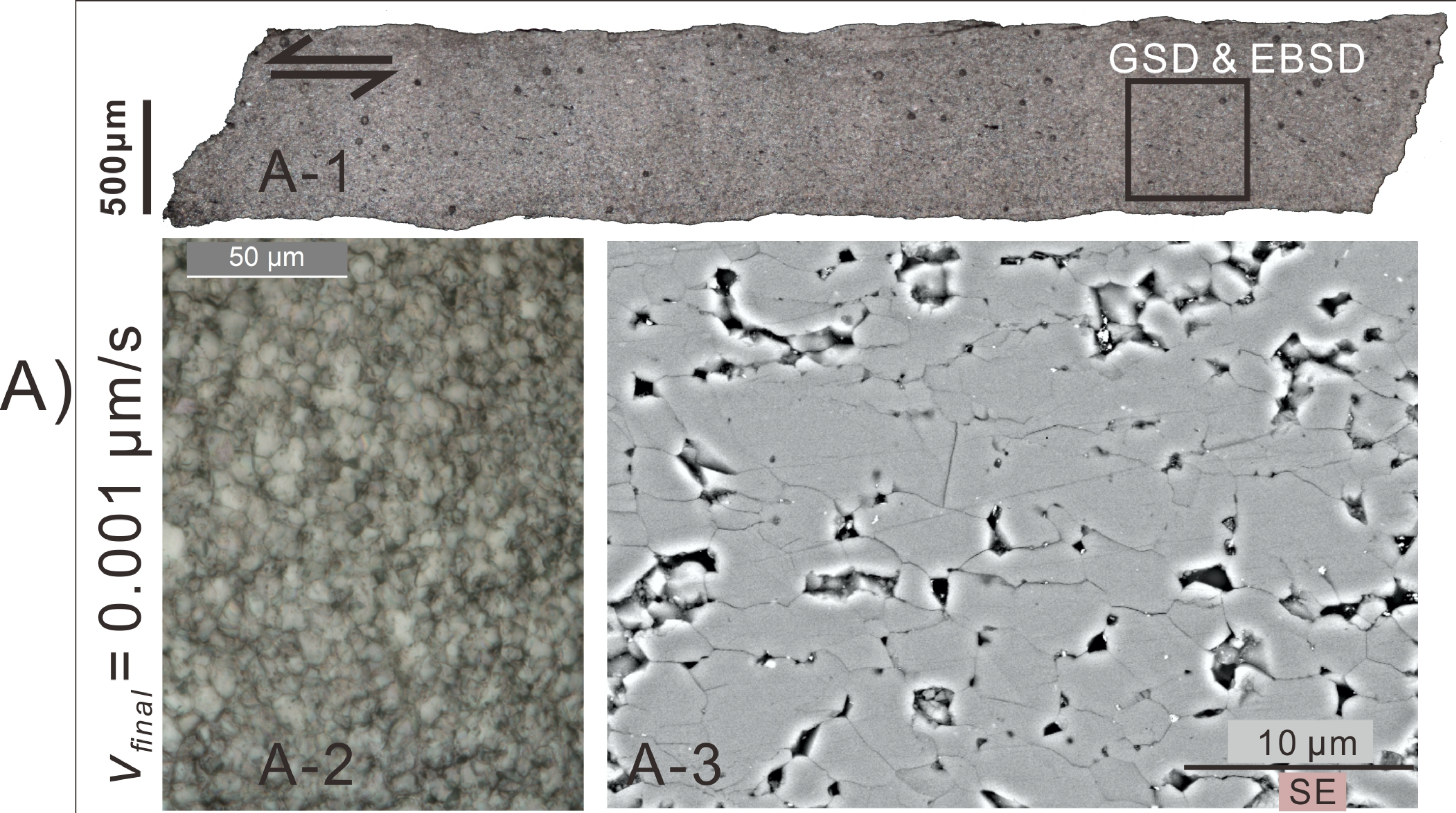


Figure 6.

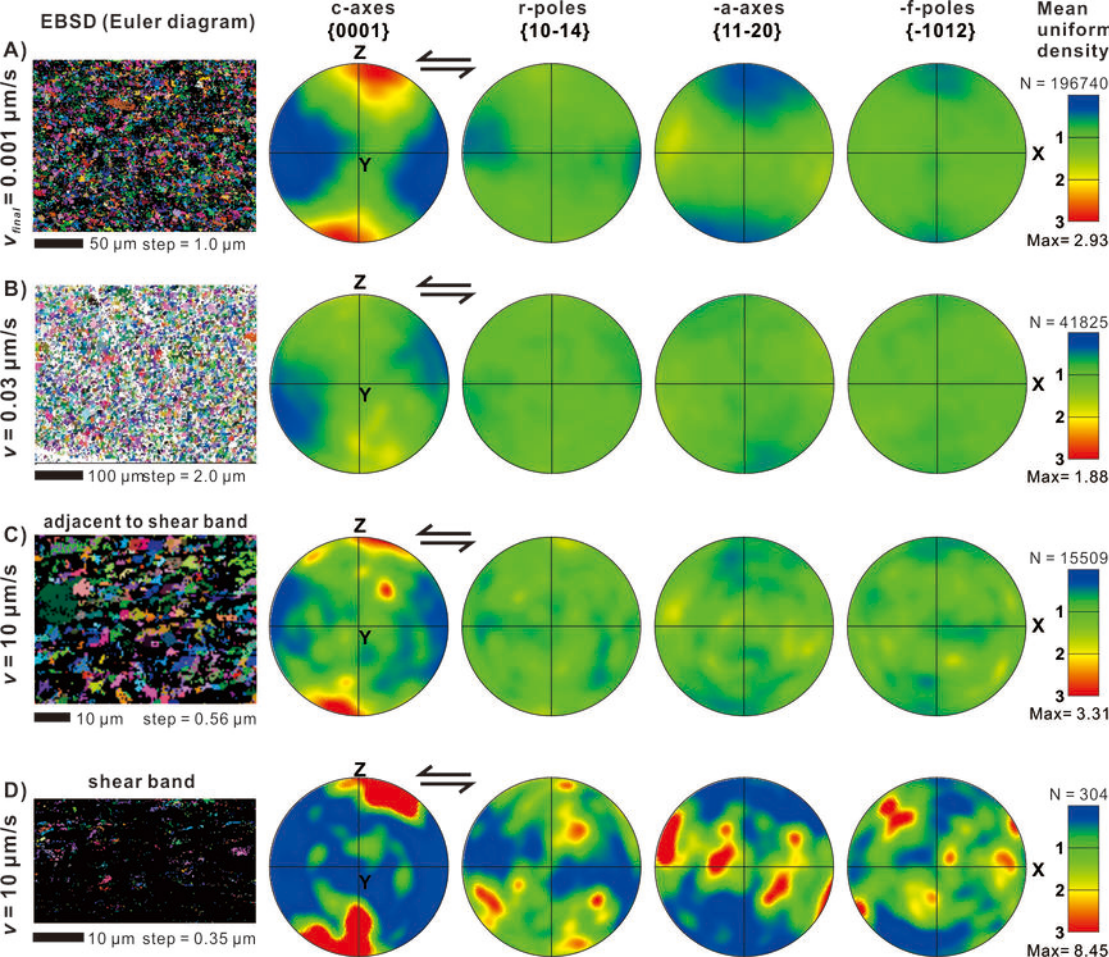


Figure 7.

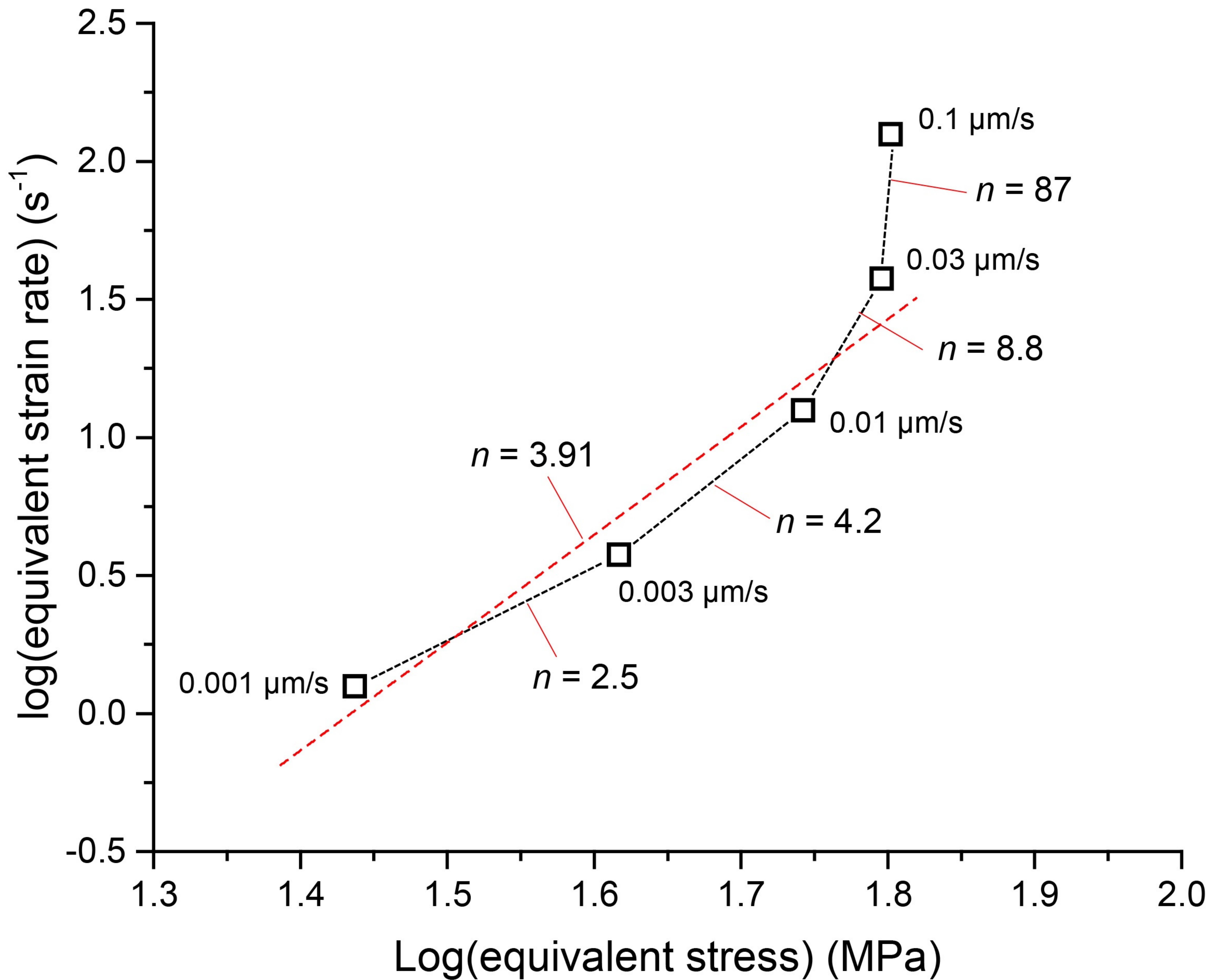


Figure 8.

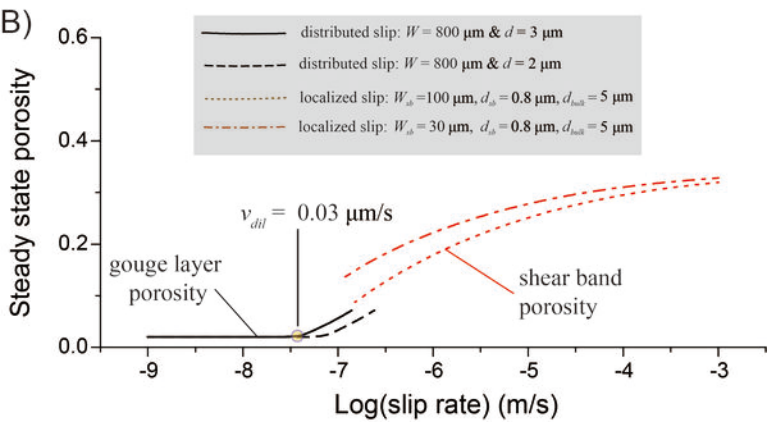
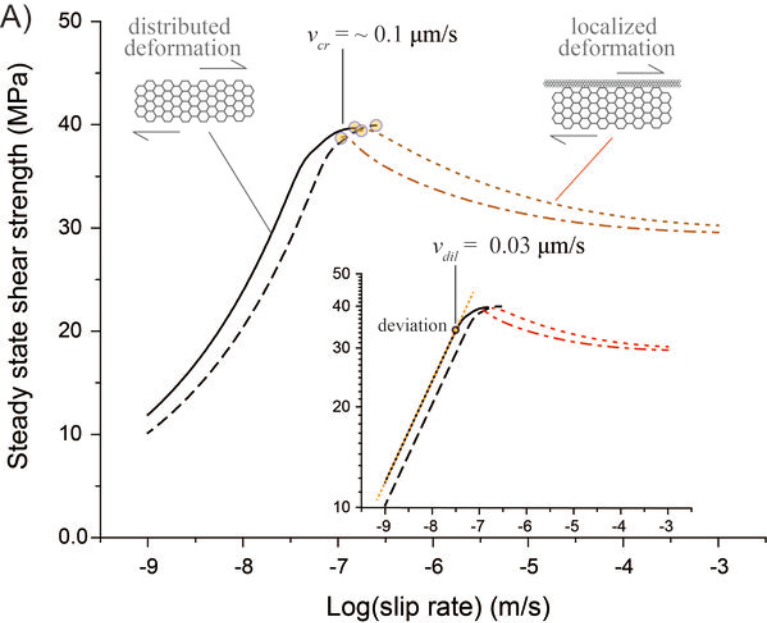


Figure 9.

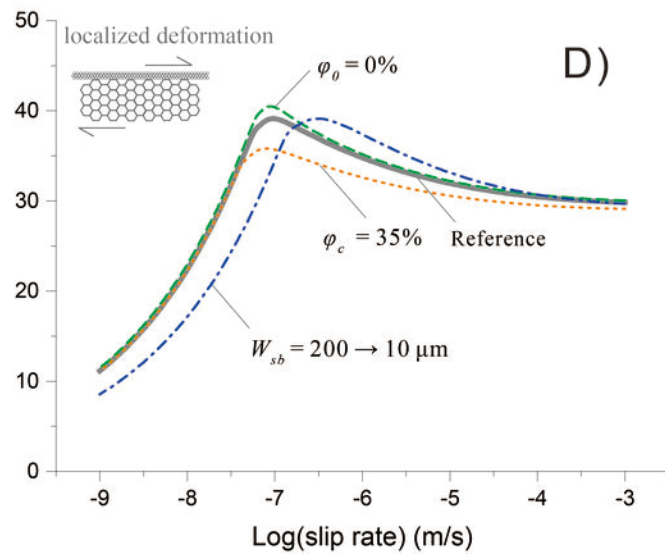
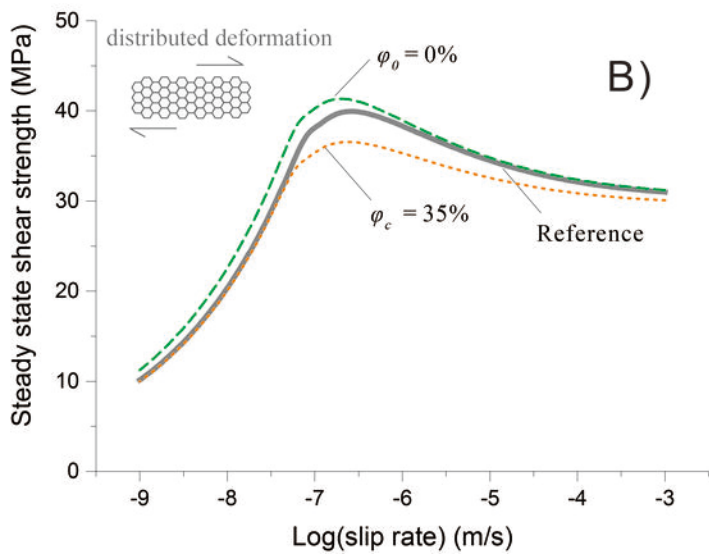
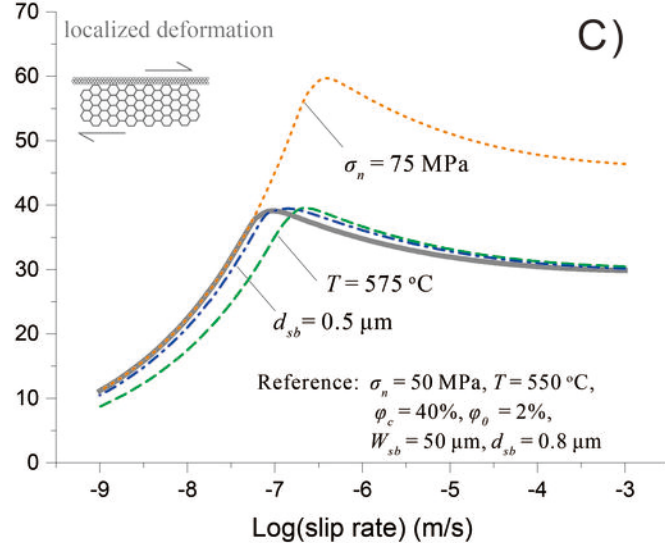
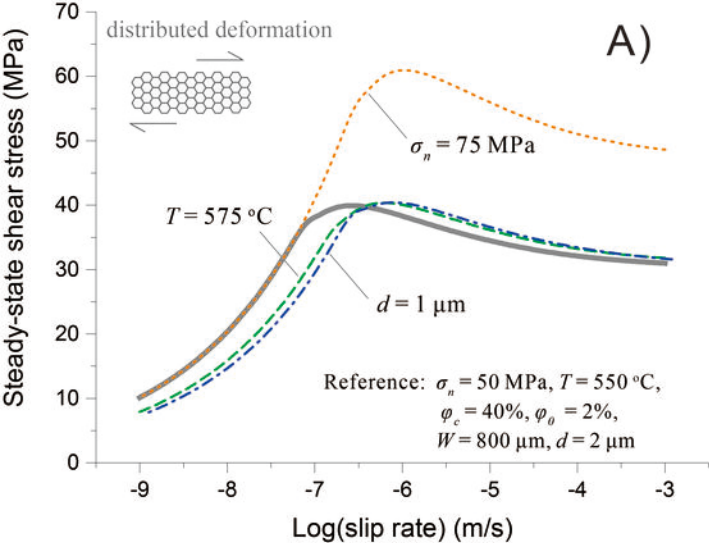


Figure 10.

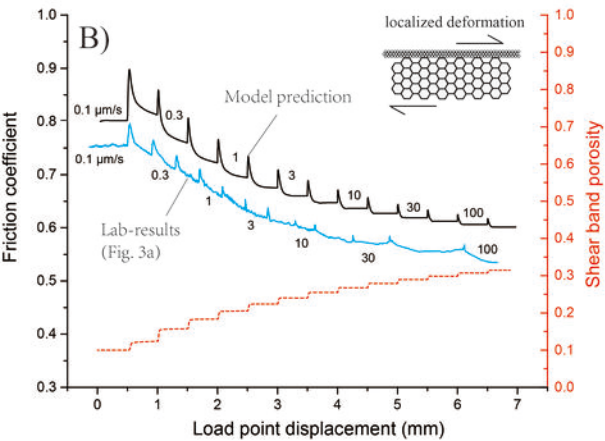
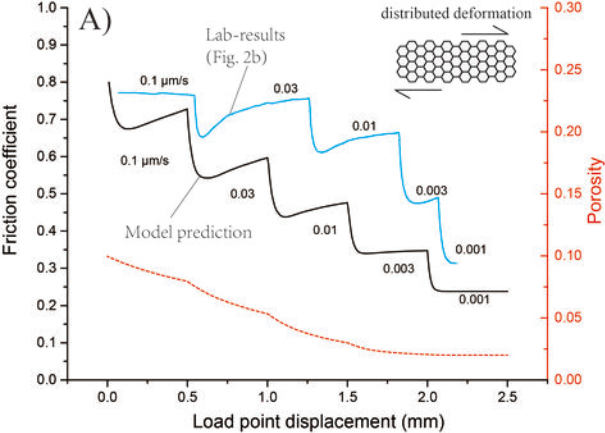


Figure 11.

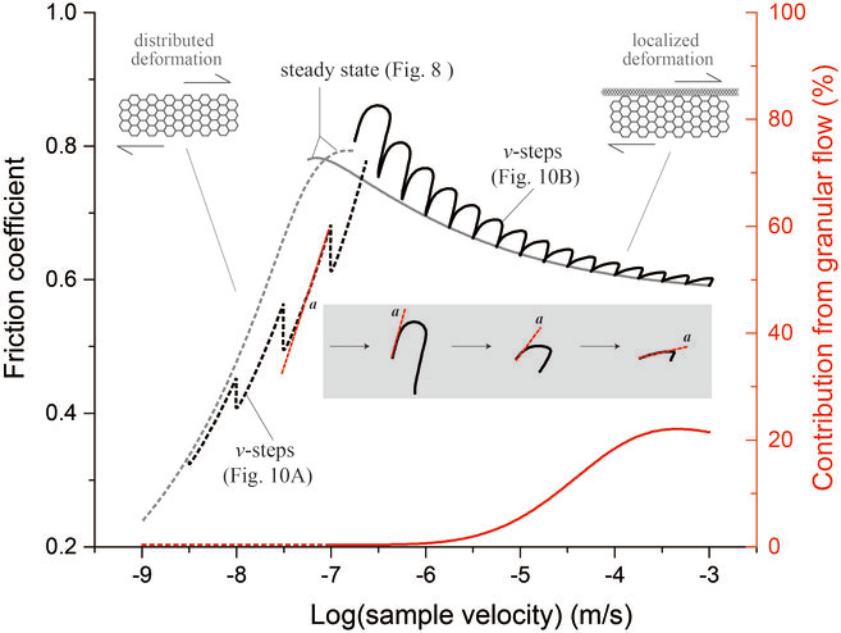
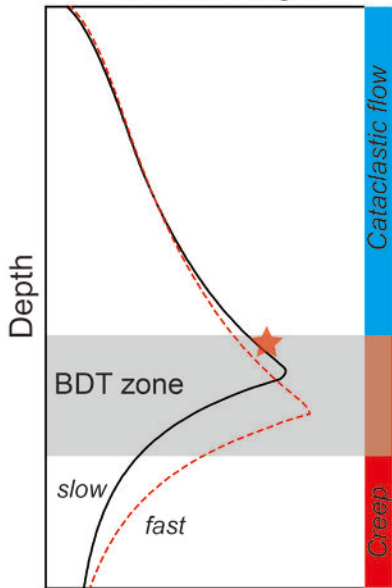


Figure 12.

A) Shear strength



B) Characterized by overprinted fault rocks

